The Astrophysical Journal, 965:35 (20pp), 2024 April 10 https://doi.org/10.3847/1538-4357/ad26f3

Modeling the Reverberation Response of the Broad-line Region in Active Galactic Nuclei

Sara A. Rosborough[1], Andrew Robinson[1], Triana Almeyda[2], and Madison Noll[3,4]
[1] Laboratory for Multiwavelength Astrophysics, School of Physics and Astronomy, Rochester Institute of Technology, 84 Lomb Memorial Drive, Rochester, NY 14623, USA
[2] Department of Astronomy, University of Florida, 211 Bryant Space Science Center Stadium Road, Gainesville, FL 32611, USA
[3] Churchville-Chili Senior High School, 5786 Buffalo Road Churchville, NY 14428, USA
[4] Research Intern, Laboratory for Multiwavelength Astrophysics, School of Physics and Astronomy, Rochester Institute of Technology, 84 Lomb Memorial Drive, Rochester, NY 14623, USA
Received 2023 June 8; revised 2024 January 31; accepted 2024 February 2; published 2024 April 2

Abstract

The variable continuum emission of an active galactic nucleus (AGN) produces corresponding responses in the broad emission lines, which are modulated by light travel delays, and contain information on the physical properties, structure, and kinematics of the emitting gas region. The reverberation mapping technique, a time series analysis of the driving light curve and response, can recover some of this information, including the size and velocity field of the broad-line region (BLR). Here we introduce a new forward-modeling tool, the Broad Emission Line MApping Code, which simulates the velocity-resolved reverberation response of the BLR to any given input light curve by setting up a 3D ensemble of gas clouds for various specified geometries, velocity fields, and cloud properties. In this work, we present numerical approximations to the transfer function by simulating the velocity-resolved responses to a single continuum pulse for sets of models representing a spherical BLR with a radiatively driven outflow and a disklike BLR with Keplerian rotation. We explore how the structure, velocity field, and other BLR properties affect the transfer function. We calculate the response-weighted time delay (reverberation "lag"), which is considered to be a proxy for the luminosity-weighted radius of the BLR. We investigate the effects of anisotropic cloud emission and matter-bounded (completely ionized) clouds and find the response-weighted delay is only equivalent to the luminosity-weighted radius when clouds emit isotropically and are radiation-bounded (partially ionized). Otherwise, the luminosity-weighted radius can be overestimated by up to a factor of 2.

Unified Astronomy Thesaurus concepts: Reverberation mapping (2019); Astronomy data modeling (1859); Supermassive black holes (1663); Active galactic nuclei (16)

Supporting material: animations

1. Introduction

Rapidly growing supermassive black holes (SMBHs) are fed by a surrounding accretion disk, which together compose the central engines of active galactic nuclei (AGNs). Most, if not all, large galaxies host an SMBH and its mass, $M_\bullet$, is closely tied to the galaxy's evolution. Decades of $M_\bullet$ estimates show a correlation to the host galaxy's stellar velocity dispersion ($\sigma_\star$), the $M_\bullet$–$\sigma_\star$ relation (McConnell & Ma 2013), implying coevolution between the SMBH and the bulge. The power of an AGN is regulated by the SMBH accretion rate, which is limited by its Eddington luminosity, where $L_{\rm Edd} \propto M_\bullet$ and $M_\bullet$ can be 10^6–10^{10} solar masses ($M_\odot$). Outflows and jets from AGNs are thought to have a profound influence on galaxy evolution by suppressing star formation. Therefore, establishing how the SMBH mass function evolves with redshift and luminosity is critical to understanding galaxy formation and evolution (Di Matteo et al. 2005; Hopkins et al. 2008; Alexander & Hickox 2012; Fabian 2012).

1.1. The Broad-line Region

The AGN's central engine is surrounded by a geometrically and optically thick structure comprising molecular gas and dust clouds, generally known as the dusty "torus" (e.g., Urry & Padovani 1995). Depending on grain composition and size, dust sublimates at temperatures between ∼1500 and 1800 K and cannot survive the heating by the accretion disk's UV/optical continuum within the corresponding dust sublimation radius, $R_d \sim 1$ pc (assuming an AGN luminosity $\sim 10^{45}$ erg s^{-1}). Inside R_d is the broad-line region (BLR), a largely dust-free zone where dense gas clouds are photoionized by the continuum radiation (e.g., Baskin et al. 2014; Baskin & Laor 2018; Amorim et al. 2021a). Residing well within the SMBH's gravitational sphere of influence, the gas clouds emit spectral lines that are Doppler-broadened by a several tens of thousand kilometers per second (e.g., Netzer 2008). The BLR is therefore a unique diagnostic of the SMBH's mass and the physical processes that operate in its environment.

The mass of the black hole, $M_\bullet$, can be estimated from the velocity dispersion (Δv) and radius ($R_{\rm BLR}$) of the BLR,

$$M_\bullet = f\frac{\Delta v^2 R_{\rm BLR}}{G} \quad (1)$$

where G is the gravitational constant (e.g., Bentz & Katz 2015). However, since AGNs are too distant and the BLR is far too small in angular size to obtain spatially resolved spectra, the BLR's structure and dynamics are not understood in detail. Therefore, the virial factor, f, accounts for the unknown geometry and kinematics, and $\Delta v^2 R_{\rm BLR}/G$ is the virial mass, $M_{\bullet,\rm vir}$ (Netzer & Marziani 2010; Pancoast et al. 2014; Homayouni et al. 2020). Comparisons of $M_{\bullet,\rm vir}$ from the AGN that have been reverberation mapped to $M_\bullet$ determined

with the $M_\bullet$–σ_* scaling relationship indicate $f \approx 4.5$ (Woo et al. 2015; Batiste et al. 2017). Δv can be estimated from broad emission-line (BEL) profile widths, but $R_{\rm BLR}$ cannot be directly determined through imaging for most AGNs (with a few exceptions discussed below). Instead, $R_{\rm BLR}$ can be determined by the reverberation mapping technique, which utilizes the response of the broad lines to the AGN's continuum variability and is not fundamentally limited by distance. BLR reverberation mapping is currently the only practical means of probing the SMBH mass function over a large range in redshift and luminosity (Shen 2013, and references therein).

Arguably the most important result from BLR reverberation mapping is the tight relationship found between the measured lag (t') and the AGN luminosity, which implies a BLR radius–AGN luminosity relationship, $t' \propto R_{\rm BLR} \propto L_{\rm AGN}^{0.5}$ (e.g., Bentz et al. 2009, 2013). This provides the key for determining $M_\bullet$ for very large samples, since both the AGN continuum flux and the BEL profile width can be measured from a single spectrum, yielding $L_{\rm AGN}$ (hence $R_{\rm BLR}$) and Δv, respectively (e.g., McLure & Jarvis 2002; Vestergaard & Peterson 2006; Liu et al. 2012).

In a few nearby and luminous AGNs, the BLR has been spatially resolved with near-infrared (NIR) interferometry. Very high-resolution interferometry observations of 3C 273, IRAS 09149-6206, and NGC 3783 have been obtained with the GRAVITY instrument using the European Southern Observatory Very Large Telescope Interferometer (VLTI). These data suggest that all three AGNs have a rotating, disklike BLR. From the broad Paschen-α line of the quasar 3C 273, Sturm et al. (2018) inferred $R_{\rm BLR} = 0.12 \pm 0.03$ pc and $M_\bullet = 2.6 \pm 1.1 \times 10^8\, M_\odot$. Amorim et al. (2020) spatially resolved the broad Brγ line in IRAS 09149-6206 and inferred $R_{\rm BLR} = 0.075$ pc and $M_\bullet \sim \times\, 10^8\, M_\odot$. More recently, Amorim et al. (2021b) used VLTI data to map broad Brγ in NGC 3783 and found a BLR with a radial distribution of clouds within $R_{\rm BLR} \approx 0.014$ pc, and then Amorim et al. (2021a) reported $M_\bullet = 2.54^{+0.90}_{-0.72} \times 10^7\ M_\odot$. For all three objects, the BLR measurements obtained from GRAVITY are consistent with the R–L relation and reverberation mapping studies of those same AGNs.

1.2. Reverberation Mapping

In the "point-source reverberation model," clouds respond to fluctuations in the continuum flux on timescales of hours, much smaller than the light-crossing time of the whole BLR, which is on the order of days to weeks. The differences in time for a photon to travel between the accretion disk, a given cloud, and then (as a line photon) to an observer means there is a corresponding time lag between the observed continuum variations and the response of the BELs. From the perspective of a distant observer, the clouds that respond at the same delay time form parabolic isodelay surfaces,

$$t' = \frac{r}{c}(1 - \cos\Theta) \tag{2}$$

where r is the cloud's radial distance from the continuum source, and Θ is the angle between the observer's line of sight (LOS) and the cloud's position vector. The observed variation of emission-line luminosity with time, t, at LOS velocity, $v^{\parallel}$, is given by the convolution of the continuum luminosity, $L_c(t - t')$, with a transfer function, $\Psi(t', v^{\parallel})$,

$$L(t, v^{\parallel}) = \int_{-\infty}^{\infty} \Psi(t', v^{\parallel}) L_c(t - t') dt' \tag{3}$$

where $L(t, v^{\parallel})$ is the velocity-resolved response of the emission line. The transfer function is the emission line's response to the continuum at $t = t'$ and encodes information about the BLR's geometry and velocity field (Blandford & McKee 1982).

Typically, $R_{\rm BLR}$ is recovered by cross-correlating the observed line light curve with the continuum light curve ($L(t)$ and $L_c(t - t')$, respectively) to measure the response-weighted time lag, $t'_{\rm RW}$, which is assumed to be equivalent to the luminosity-weighted radius of the BLR; $R_{\rm LW} \approx ct'_{\rm RW}$ (Robinson & Perez 1990; Koratkar & Gaskell 1991; Pérez et al. 1992; Almeyda et al. 2020). The value of $R_{\rm LW}$ inferred is then used in Equation (1) to find the SMBH mass; i.e., $R_{\rm BLR} = R_{\rm LW}$. However, due to the complex properties of the BLR, $ct'_{\rm RW}$ is not necessarily an accurate estimate of $R_{\rm BLR}$. As part of this work, we compare the relation between the $ct'_{\rm RW}$ and $R_{\rm LW}$ values for our BLR models to understand how well the measured lag represents $R_{\rm LW}$.

1.3. Modeling Reverberation Responses

As discussed by Mangham et al. (2019), methods for deciphering the structure and kinematics of the BLR from velocity-resolved reverberation mapping data fall into two categories. First, in the "inverse" method, the transfer function can be recovered from data using deconvolution techniques, such as the maximum entropy method (MEM) used in the MEMECHO code by Horne et al. (2004). Deconvolving the transfer function accurately from an observed response is not easily done, as it requires very well-sampled data over a sufficiently long observing period. Furthermore, if the transfer function is reliably obtained, deciphering the BLR's geometry and velocity parameters is not a straightforward task, since they would have to be inferred from the shape of the transfer function, which would probably require modeling. The other method is forward modeling, which is the approach used by the Code for AGN Reverberation and Modeling of Emission Lines (CARAMEL) by Pancoast et al. (2011), the BLR Reverberation-mapping Analysis In AGNs with Nested Sampling (BRAINS) by Li et al. (2013) and, for the dusty torus, the TOrus Reverberation MApping Code (TORMAC) by Almeyda (2017). These BLR computer simulations predict $L(t, v^{\parallel})$, given an input, driving light curve. The simulated response light curves and BEL profiles for different BLR configurations can then be compared to observed AGN light curves and time-domain spectra. Here we present a new forward-modeling code adopted from TORMAC, the Broad Emission Line MApping Code (BELMAC), which generates the velocity-resolved response for various BLR geometrical configurations, gas properties, cloud distributions, and velocity fields, given any input light curve.

BELMAC models the BLR as an ensemble of discrete clouds, whose line emission is calculated using nebular physics. We used hydrogen recombination theory for the models presented in this paper, but a large grid of photoionization models will be used in the forthcoming version. In contrast, CARAMEL utilizes a more prescriptive parameterization of BLR properties. For example, CARAMEL treats the clouds as particles that are representative of a gas density field and approximates the responding emission by

setting the emissivity as a radial power-law function (Williams & Treu 2022). CARAMEL includes a parameter estimation procedure to recover the best-matching model for a time series data set, which is not yet implemented in BELMAC. BRAINS is based on CARAMEL and therefore employs similar methodology. However, BRAINS allows the BLR emission to respond nonlinearly, and Li et al. (2018) added a two-zone BLR geometry, where each zone may have a different cloud distribution, which could be used to model a disklike BLR with a wind. BELMAC may also be used to model a two-zone BLR, with different gas density and cloud distributions, velocity fields, and radial sizes, but we leave this discussion for a future paper.

Other numerical reverberation mapping studies of the velocity-resolved response have been performed by Welsh & Horne (1991), Pérez et al. (1992), Robinson (1995), and Peterson & Horne (2004). Building on the hydrodynamics simulations of various BLR models with a disk and wind component by Proga & Kallman (2004), Waters et al. (2016) presented a radiative transfer methodology to create the corresponding velocity-resolved reverberation response. As noted by Waters et al. (2016), reverberation mapping modeling codes would ideally include a detailed treatment of hydrodynamics, incorporating radiative transfer, and photoionization physics. However, these codes do not yet exist and would no doubt be computationally expensive.

Our overall goal in developing BELMAC is to create a fast and flexible code that can be used to generate large model grids to fit reverberation mapping observations. However, it is useful to understand how various properties of the BLR affect the reverberation response (e.g., Welsh & Horne 1991; Pérez et al. 1992; Horne 1994). In this paper, we introduce the basic features of BELMAC and explore the effects of parameters controlling the BLR geometry, kinematics, and cloud properties on the velocity-resolved transfer function. As our main focus here is on the general properties of the BLR, we simplify the calculation of the line emission by using hydrogen recombination theory. A narrow square-wave pulse is used as the driving light curve to produce a numerical approximation of the transfer function.

BELMAC is outlined in Section 2 with a description of the geometry setup, velocity field, and the calculation of the cloud emission. In Section 3 we present our results for two example models, a spherical BLR with a radiative pressure driven radial outflow and a rotating thin disk. We discuss how our simple reprocessing models can help us understand the behavior of responses and time-domain spectra, the parameters that affect measured time lags, and the future development planned for BELMAC in Section 4. Finally, we summarize our conclusions in Section 5.

2. Outline of the Code: BELMAC

The BLR is represented as a 3D ensemble of discrete clouds, that are randomly distributed within a defined structure. BELMAC follows the same geometry setup as TORMAC described in Almeyda et al. (2017), but the clouds within the ensemble are dust-free, photoionized gas clouds and have velocities specified by various choices of velocity field. The general flow of BELMAC is illustrated in Figure 1 and described in detail in the following subsections. The user provides the AGN's bolometric luminosity, $L_{\rm AGN}$, spectral energy distribution (SED), and driving light curve. The geometry, velocity field, and distribution of the ensemble of BLR clouds are described by $Y_{\rm BLR}$, σ, i, C_f, s, p, and $M_{\bullet}$. The cloud positions are randomly generated, and each cloud's LOS velocity is calculated based on the type of velocity field specified, either Keplerian, radial flow, or turbulent. In all, there are 10 descriptive parameters for each distinctive BLR model.

BELMAC can use any input light curve, but in order to obtain a numerical approximation of the transfer function, the input light curve is a single square-wave pulse to represent a δ-function. We refer to the approximate transfer function as the response function (Almeyda et al. 2017). For the duration of the pulse, $\sim$4 days, the ionizing luminosity increases by a factor of 2. The light-front corresponding to the light pulse propagates outward from the center of the system with time, and the total luminosity of the BLR is computed by integrating over the cloud ensemble at each observer time step, taking into account light travel delays. Table 1 summarizes all of the BELMAC parameters with their respective descriptions, symbol, and values we used for the BLR models presented in this paper.

2.1. BLR Geometry and Cloud Structure

In common with many other studies (e.g., Davidson & Netzer 1979; Robinson & Perez 1990; Marconi et al. 2008; Armijos-Abendaño et al. 2022), we assume that the BLR gas is distributed in many small clouds. Cloud positions are defined by the spherical polar coordinates r, θ, ϕ, where r is the radial distance from the continuum source at the origin, θ is the polar angle, and ϕ is the azimuthal angle. In the models considered here, the BLR is assumed to have "sharp" boundaries with the clouds uniformly distributed in elevation above the equatorial plane, $90^\circ - \theta$, and in ϕ. However, "fuzzy" edges may also be arranged by drawing values of the elevation angle from a Gaussian distribution (Figure 2; Almeyda et al. 2017). The disk's angular width is set by the half-angle σ, where $\sigma = 90^\circ$ is a spherical ensemble. The inclination, i, is the angle between the polar axis and the observer's LOS; therefore, for $i = 0^\circ$, the disk is viewed face-on, and for $i = 90^\circ$ it is viewed edge-on (Figure 2).

The outer radius of the BLR is set by the dust sublimation radius, R_d,

$$R_d = 0.4\left(\frac{L_{\rm AGN}}{10^{45}\ {\rm erg\ s^{-1}}}\right)^{1/2}\left(\frac{1500\ K}{T_{\rm sub}}\right)^{2.6}{\rm pc} \quad (4)$$

where $T_{\rm sub}$ is the dust sublimation temperature (Nenkova et al. 2008a). Here we take the representative values, $L_{\rm AGN} = 10^{45}$ erg s^{-1} and $T_{\rm sub} = 1500$ K, then $R_d \approx 10^{18}$ cm (0.4 pc). For simplicity, we will treat the dust sublimation radius as a sharp boundary between the BLR and torus, rather than as a transition region, which would be more physically realistic (Baskin & Laor 2018). The inner radius of the BLR, $R_{\rm in}$, is set by the free parameter $Y_{\rm BLR} = R_d/R_{\rm in}$. In all of the models presented here, we will use $Y_{\rm BLR} = 20$, similar to scaled sizes used in previous modeling (e.g., Du et al. 2015; Netzer 2020). This gives $R_{\rm in} \approx 6 \times 10^{16}$ cm (0.02 pc), which corresponds to a light-crossing time of $\sim$24 days. This is consistent with observed BLR time lags that range from days to $\sim$a month (e.g., Fausnaugh et al. 2017) and the R–L relation (Bentz et al. 2013).

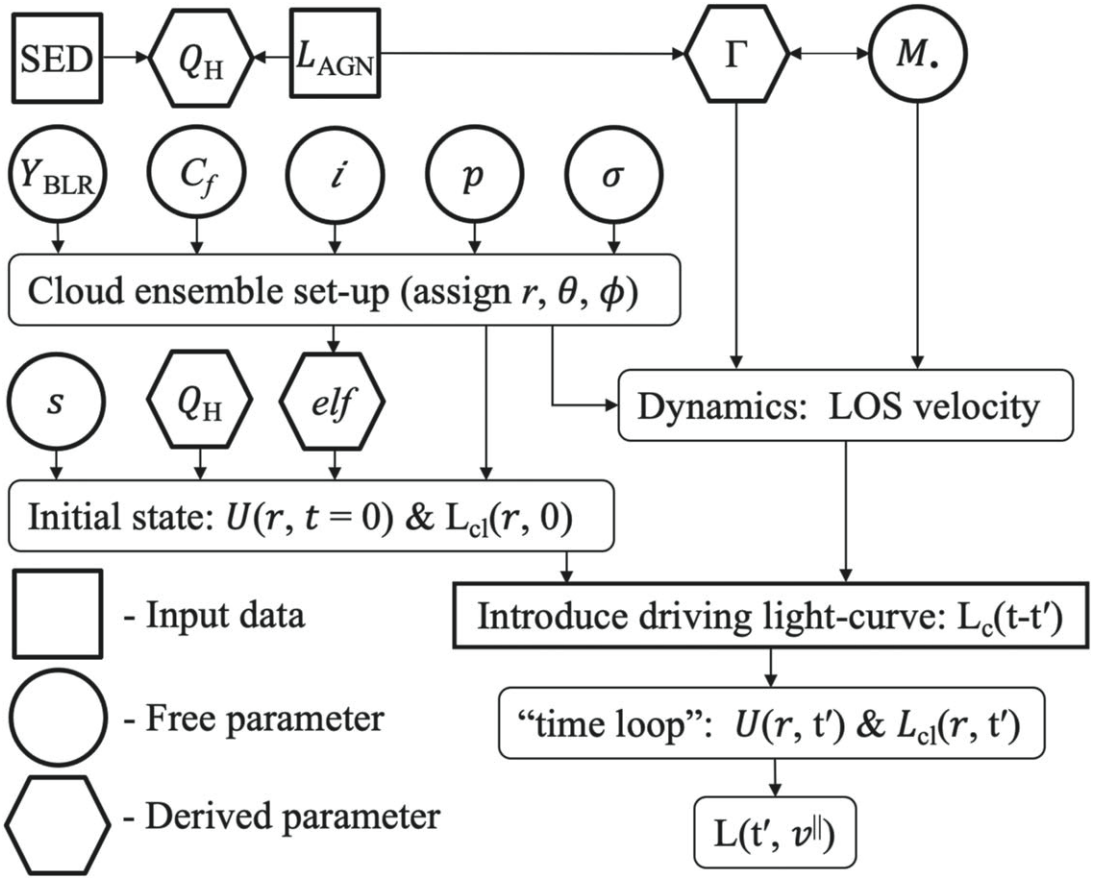

Figure 1. A summary of BELMAC's operation. The parameters are explained in Section 2 and listed in Table 1. The parameters in bolded squares are input data provided by the user. The free parameters in circles determine the BLR model setup, and parameters in hexagons are calculated within the code. The final output of the code is the velocity-resolved response, $L(t, v^{||})$.

Table 1
BLR Geometry and Property Parameters Used to Set Up the Ansemble and Their Value(s) Used in the Models Presented in This Paper

Parameter Description	Symbol	Model Values
Bolometric luminosity	L_{AGN}	10^{45} erg s^{-1}
Total ionizing photon luminosity[a]	$Q_H(R_d, t' = 0)$	2.6×10^{55} photons s^{-1}
black hole mass	$M_\bullet$	$10^8\ M_\odot$
Eddington ratio	Γ	0.07
Ionizing to total luminosity ratio	α_f	0.5
Outer radius	R_d	1.23×10^{18} cm
Size scaled to R_d	Y_{BLR}	20
Angular width	σ	15°
Cloud distribution power-law index	p	0, 1, and 2
Total number of clouds	N_{tot}	100,000
Inclination to observer	i	0°–90°
Covering fraction	C_f	0.3
Cloud sizes	$R_{cl}(r)$	$10^{12} - 10^{14}$ cm
Gas density in a cloud at R_d	$n(R_d)$	10^9 cm^{-3}
Power-law index for gas density	s	0, −1, & −2
Emission-line fraction[b]	elf	0–1

Notes.
[a] Calculated from the SED model of Jin et al. (2012) for $M_\bullet = 10^8\ M_\odot$ and $\Gamma = 0.1$. See their Figure 14, panel 4-C.
[b] Not a free parameter, but can be turned on or off.

The radial cloud distribution is given by a power law with index p, such that the number of clouds between r and $r + dr$ is

$$N(r)dr = A_o\left(\frac{r}{R_d}\right)^p dr, \tag{5}$$

where A_o is a normalization constant that is determined by the total number of clouds, $N_{tot} = \int_{R_{in}}^{R_d} N(r)dr$ (Almeyda et al. 2017). The BLR clouds are assumed to be spherical, with radii, $R_{cl}(r)$, specified by the integrated covering fraction of the BLR,

$$C_f = \int_{R_{in}}^{R_d} \frac{N(r)}{4\pi r^2} A_{cl}(r) \sin\sigma dr \tag{6}$$

where the cloud's cross-sectional area is $A_{cl}(r) = \pi R_{cl}^2(r)$. We assume the clouds are composed of pure hydrogen and have a constant mass, $m_{cl}(r) = m_{cl}$. Realistically, the mass of the clouds could change with distance depending on how the clouds are confined, such as by radiation pressure or magnetic fields. For a pure hydrogen gas cloud, the ionized portion of the cloud has an electron density equal to the hydrogen density, which is the cloud's gas density $n(r)$. The gas density is a power-law function of the cloud's radial distance from the continuum, $n(r) = n_o(r/R_d)^s$, where the values of the gas density at the outer radius of the BLR, $n(R_d) = n_o$, and the power-law index, s, are free parameters. Therefore, the cloud

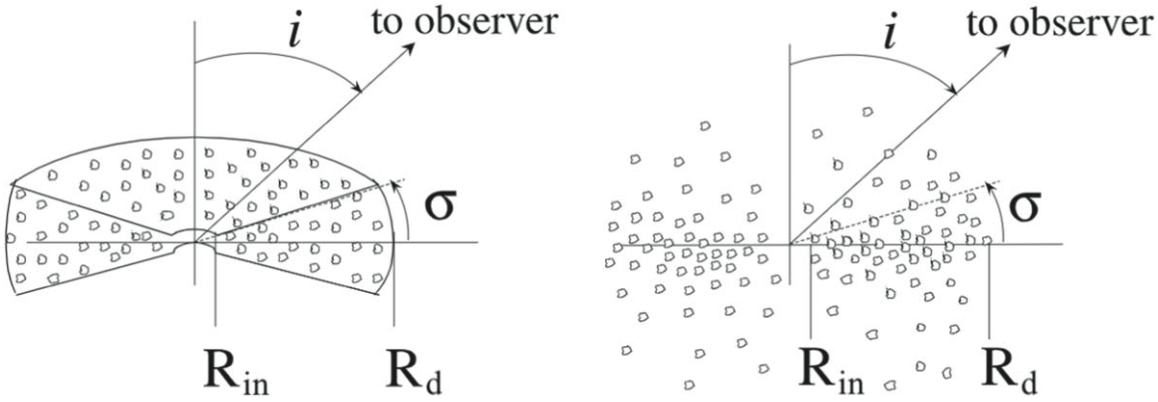

Figure 2. Geometrical parameters used for clouds arranged in a flared disk in BELMAC. $R_{\rm in}$ and R_d are the inner and outer radii, σ is half-angle width of the disk, and i is the inclination of the disk axis to the observer's line of sight (LOS). On the left is a sharp-edged BLR configuration and a "fuzzy" (Gaussian distribution in β) boundary is shown on the right. Adapted from Nenkova et al. (2008b).

radius $R_{cl}(r) \propto r^{-s/3}$ and the cloud column density,

$$N_c(r) \propto R_{cl}(r) n(r) \propto r^{2s/3} \tag{7}$$

will vary with distance from the ionizing source (Netzer 2008).

2.2. Cloud Emission

To approximate the Hα luminosity of a cloud, we use hydrogen recombination theory (Osterbrock & Mathews 1986). For spherical clouds, $d_c(r)$ is the average path length through the cloud, which is proportional to $R_{cl}(r)$. The surface of a cloud facing the source is exposed to the ionizing flux and is entirely ionized. Assuming ionization equilibrium, the clouds are fully ionized within the Strömgren depth,

$$d_s(r) = \frac{cU(r, t')}{n(r)\alpha_B} = N_s(r)/n(r) \tag{8}$$

where α_B is the recombination coefficient for hydrogen ($\alpha_B \approx 2.6 \times 10^{-13}$ cm^3 s^{-1}; Osterbrock & Mathews 1986) and $N_s(r)$ is the Strömgren column density. The ionization state of a given cloud is described by the ionization parameter, the ratio of the local ionizing photon flux, $\Phi(r, t')$, to the cloud's gas density,

$$U(r, t') = \frac{\Phi(r, t')}{cn(r)} = \frac{Q_{\rm H}(t')}{4\pi r^2 cn(r)} \propto r^{-s-2} \tag{9}$$

where $Q_{\rm H}(t')$ is the total ionizing photon luminosity. Since the continuum luminosity naturally undergoes temporal variability, $Q_{\rm H}(t')$ and, hence, $U(r, t')$ fluctuate with time. $Q_{\rm H}(t' = 0)$ is obtained from any selected AGN's SED and $L_{\rm AGN}$, which sets $U(R_d, 0)$. To estimate $Q_{\rm H}(0)$, for the models presented in this paper, we use the compiled SED created by Jin et al. (2012), who constructed an average SED using 17 type 1 AGNs that have an average Eddington ratio $\Gamma = 0.07$ and $M_\bullet = 10^8\ M_\odot$.

If $d_s \geqslant d_c$, the cloud is fully ionized, or "matter-bounded," and has reached its maximum ability to emit hydrogen recombination line radiation. Otherwise a cloud is partially ionized and "radiation-bounded." The cloud luminosity for radiation and matter-bounded clouds is, respectively,

$$L_{cl} = \begin{cases} n(r)^2 \alpha_{\rm H\alpha}^{\rm eff} h\nu_{\rm H\alpha} \pi R_{cl}^2(r) d_s(r) & \text{for } d_s < d_c \\ n(r)^2 \alpha_{\rm H\alpha}^{\rm eff} h\nu_{\rm H\alpha} \pi R_{cl}^2(r) d_c(r) & \text{for } d_s \geqslant d_c \end{cases} \tag{10}$$

where $\alpha_{\rm H\alpha}^{\rm eff}$ is the effective recombination coefficient for Hα ($\alpha_{\rm H\alpha}^{\rm eff} \approx 1.1 \times 10^{-13}$ cm^3 s^{-1}). In the matter-bounded case for constant mass clouds, the cloud luminosity $L_{cl}(r) \propto n(r) \propto r^s$, but it is independent of $U(r, t')$ and therefore is not time-dependent. In the radiation-bounded case, the cloud luminosity does depend on $U(r, t')$ and thus $L_{cl}(r, t') \propto n(r) A_{cl}(r) U(r, t') \propto r^{-2(1+s/3)} Q_{\rm H}(t')$. The cloud luminosities are summed at each time interval in the observer's frame to calculate the total BLR luminosity as a function of time.

At the high densities of the BLR, some emission lines, such as the Balmer lines, may become optically thick (Osterbrock & Mathews 1986). It is also possible that dust grains may survive in the cooler, largely neutral gas beyond the ionization front (e.g., Baskin & Laor 2018), causing extinction of line radiation produced in the ionized zone. As a result, the line emission of a cloud may vary strongly between the illuminated and nonilluminated faces. To account for this effect, BELMAC includes an approximate treatment of anisotropic cloud emission (ACE), which is dependent on a cloud's location with respect to the continuum source and the observer's LOS. Each cloud's luminosity is multiplied by its emission-line fraction (*elf*),

$$elf = \begin{cases} \frac{1}{\pi} \arccos(\sin\theta \cos\phi) & \text{for } d_s < d_c \\ 1 & \text{if } d_s \geqslant d_c \end{cases}, \tag{11}$$

which is the fraction of the illuminated side an observer sees. However, if a cloud is matter-bounded ($d_s \geqslant d_c$), then we assume that it has isotropic cloud emision (ICE) and set $elf = 1$. Figure 3 shows from the observer's perspective how the *elf* changes the cloud's luminosity with position.

We summarize the parameters governing a cloud's emission and internal properties, along with their typical values in Table 1. The ranges in s and p listed in Table 1 were chosen to encompass contrasting special cases in the gas density and cloud density distributions, respectively. Thus, when $s = 0$, the gas density is constant, but $U(r) \propto r^{-2}$ and $d_s(r) \propto r^{-2}$. The ionized fraction of a cloud therefore decreases strongly with r.

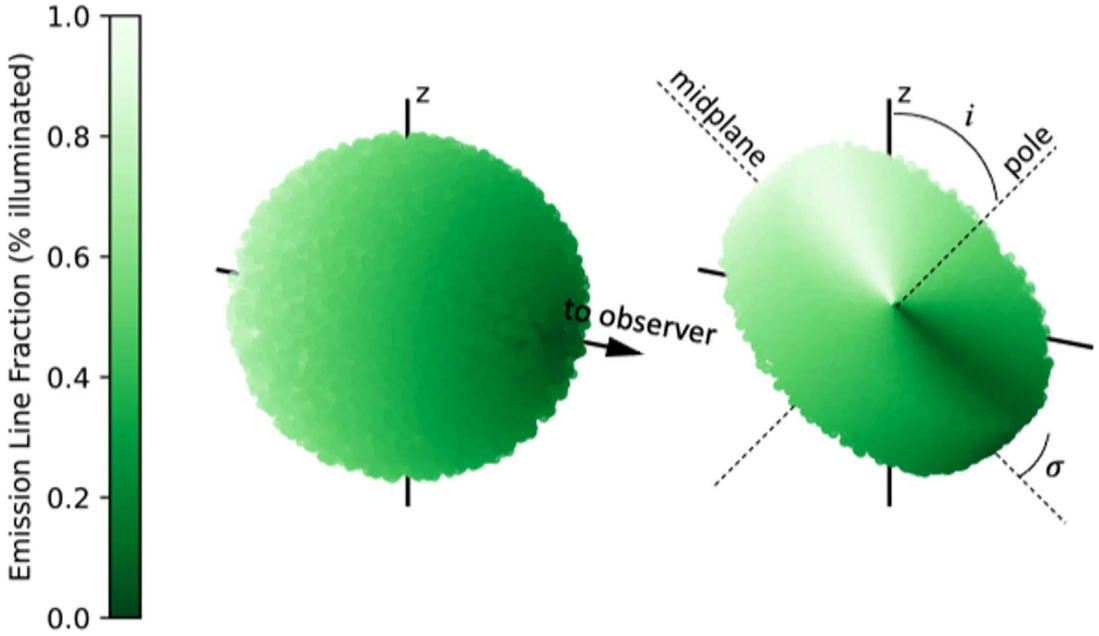

Figure 3. Two geometrical BLR configurations explored in this paper: a sphere and thin disk ($i = 45°$, $\sigma = 15°$). The color represents the *elf* parameter. The darkest green means the observer views only the nonilluminated face of the cloud. The white means the observer sees only the fully illuminated side of the cloud. Intermediate shades indicate the fraction of the illuminated side see by the observer.

Conversely, when $s = -2$, $n(r) \propto r^{-2}$ while $U(r)$ and d_s are both constant throughout the BLR. The case of $p = 0$ corresponds to $N(r) =$ constant, meaning that the clouds are centrally concentrated since the number density $\propto$ constant$/4\pi r^2$. However, when $p = 2$, the clouds are uniformly distributed throughout the BLR.

2.3. The Analytical Transfer Function

To understand how the basic features of the response function are influenced by the size of the BLR, the gas density, and radial cloud distribution, we discuss the analytical transfer function for a spherical shell. The radial cloud distribution and internal cloud properties determine the volume emissivity, $\varepsilon_V(r) \propto L_{cl}N(r)/r^2$, which will affect the shapes of the line profile and transfer function. We adopt Pérez et al.'s (1992) assumption that the cloud's emission efficiency behaves as a power law with distance and approximate the volume emissivity as

$$\varepsilon_V(r) = \varepsilon_o(r/R_{\rm in})^{\eta}, \tag{12}$$

where $\varepsilon_o = \varepsilon_V(R_{\rm in})$, and the emissivity index η relates to our p and s indices (from Equations (5) and (7), respectively) as,

$$\eta = \begin{cases} p - 4 - 2s/3 & \text{for } d_s < d_c \\ p - 2 + s & \text{for } d_s \geqslant d_c \end{cases} \tag{13}$$

for radiation and matter-bounded clouds, respectively. Recalling Equations (2) and (3), the analytical transfer function is given by

$$\Psi(t') = \int_V \varepsilon_V(r)\delta(t - t')dV, \tag{14}$$

where V is the volume of the BLR. Solving Equation (14) for a spherical shell BLR model we arrive at

$$\Psi(\tau) \propto \begin{cases} Y_{\rm BLR}^{\eta+2} - 1 \text{ for } \tau \leqslant 1/Y_{\rm BLR} \ \ \& \ \eta \neq -2 \\ Y_{\rm BLR}^{\eta+2}(1 - \tau^{\eta+2}) \text{ for } \tau > 1/Y_{\rm BLR} \ \ \& \ \eta \neq -2 \end{cases} \tag{15}$$

and

$$\Psi(\tau) \propto \begin{cases} \ln Y_{\rm BLR} \text{ for } \tau \leqslant 1/Y_{\rm BLR} \ \ \& \ \eta = -2 \\ \ln 1/\tau \text{ for } \tau > 1/Y_{\rm BLR} \ \ \& \ \eta = -2 \end{cases}, \tag{16}$$

where $\tau = ct'/2R_d$ is the delay in units of the light-crossing time of the BLR, such that the line response is complete when $\tau = 1$ (Robinson & Perez 1990; Pérez et al. 1992; Almeyda et al. 2017). In terms of τ, the duration of the square-wave pulse used in our models is 0.004.

2.4. Response-weighted Delay and Luminosity-weighted Radius

As mentioned in Section 1.2, the response-weighted time delay determined from reverberation mapping is considered a reasonable estimate of the radial extent of the BLR, $ct'_{\rm RW} \approx R_{\rm LW} = R_{\rm BLR}$. However, it is unclear how accurate this assumption is due to the uncertain and complex cloud properties of the BLR. Robinson & Perez (1990) defined the dimensionless, response-weighted delay (RWD) as,

$$\text{RWD} = \frac{\int_0^1 \tau\Psi(\tau)d\tau}{\int_0^1 \Psi(\tau)d\tau} \tag{17}$$

to characterize the delay associated with the transfer function. This is related to the cross-correlation lag as $t'_{\rm RW} = 2R_d$ RWD $/c$ in physical units. For a spherical shell containing isotropically emitting clouds, the RWD is exactly the dimensionless luminosity-weighted radius (LWR),

$$\text{LWR} = \frac{\int_V r\varepsilon_V dV}{2R_d \int_V \varepsilon_V dV} \tag{18}$$

and $R_{\rm BLR} = 2R_d$ LWR (Robinson & Perez 1990; Almeyda et al. 2020). The analytical LWR and RWD/LWR for spherical shell

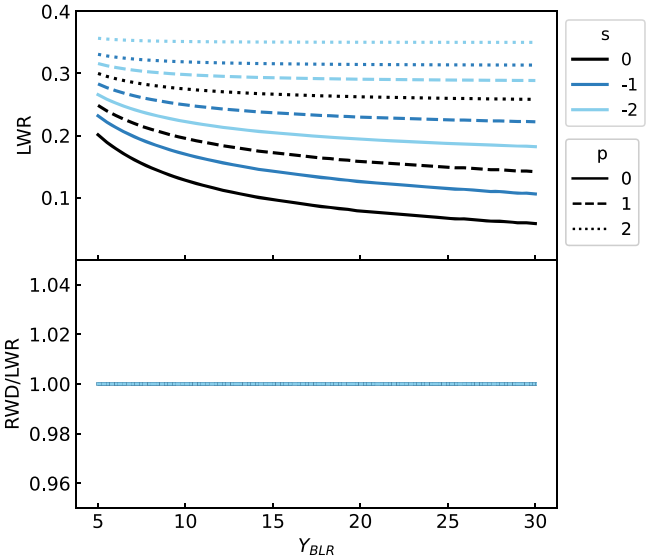

Figure 4. The analytical LWR (top row) and ratio RWD/LWR (bottom row) for a spherical shell for varying combinations of s and p parameters with $Y_{\rm BLR}$.

BLRs with varying $Y_{\rm BLR}$, s, and p are shown in Figure 4. We will present and compare the LWR and RWD of BLR models with combinations of $s = 0, -1$, and -2 and $p = 0$, 1, and 2 in Section 3.

2.5. BLR Cloud Dynamics

In order to compute the velocity-resolved response, we include three types of velocity fields: rotational, radial, and random turbulence. The broadest line widths observed are $\lesssim 0.1c$ (e.g., Assef et al. 2011; Fausnaugh et al. 2017); hence, the dynamical timescale of the BLR is much greater than ($\gtrsim 10\times$) its light-crossing time. Therefore, we assume the clouds are static as they do not significantly move along their trajectories over timescales typically of interest for reverberation mapping.

BELMAC is capable of combining radial, rotational, and random motions for a multicomponent velocity field. However, for the purposes of this paper, we will present and discuss each type of motion separately. Furthermore, we will not explore the random, turbulent motion in the models presented here.

2.5.1. Rotational Velocity Field

In the rotating disk BLR, the clouds are assumed to follow circular, Keplerian motion, $v_{\rm Kep}(r) = (GM_\bullet/r)^{1/2}$. The rotational velocity is scaled to the velocity at the inner radius,

$$v_{\rm rot}(r) = v_{\rm Kep}(R_{\rm in})(r/R_{\rm in})^{-1/2} \tag{19}$$

for a cloud at radius, r. The cloud orbits are randomly inclined relative to the disk's midplane and are constrained by the disk angular width, σ, which requires $90^\circ - \sigma \leqslant |\theta| \leqslant 90^\circ + \sigma$. Given a cloud with coordinates r, θ, and ϕ and a BLR inclination i, the velocity component along the LOS velocity to an observer is

$$v^{\parallel}_{\rm Kep} = -v_{\rm rot}(r)(\cos\theta\,\sin\phi\,\cos i - \sin\theta\,\sin\phi\,\sin i). \tag{20}$$

If we combine Equations (2) and (20) for an infinitesimally thin disk ($\sigma \to 0$, $\theta = 90^\circ$),

$$\left(\frac{v^{\parallel}_{\rm Kep}}{v_{\rm rot}\sin i}\right)^2 + \frac{(t' - (r/c))^2}{(r/c\ \sin\ i)^2} = 1 \tag{21}$$

we find the response for a given orbital radius in the projected velocity and time delay space forms an ellipse. The ellipses are centered at ($t' = r/c$, $v^{\parallel}_{\rm Kep} = 0$), with semi-axes $\pm v_{\rm rot}\sin i$ in velocity and $r/c\,\sin i$ in time delay (Welsh & Horne 1991; Pérez et al. 1992).

2.5.2. Radial Velocity Field

The radial motion is dependent on the primary outward driving mechanism, assumed here to be radiation pressure, and the inward pull of gravity. We further assume that the BLR intercloud medium is sufficiently tenuous that we can ignore the forces due to drag and the pressure gradient between the clouds. We follow the presciption of Marconi et al. (2008) and Netzer & Marziani (2010) for clouds accelerated by radiation pressure due to Thomson scattering and absorption of ionizing radiation emanating from the accretion disk.

The equation of motion for a cloud of pure hydrogen gas at a distance r from the radiation source, with cross-sectional area $A_{cl}(r)$ and mass m_{cl} is

$$a(r) = \frac{A_{cl}(r)\alpha_f L_{\rm AGN}}{4\pi r^2 m_{cl} c} - \frac{GM_\bullet}{r^2} \tag{22}$$

where $\alpha_f \simeq \int_{\nu_H}^{\infty} L_\nu d\nu \Big/ L_{\rm AGN}$, the fraction of the AGN's bolometric luminosity that is absorbed by the cloud. Although the absorption fraction will vary with $U(r, t')$ and $N_c(r)$, in this paper we use the constant value $\alpha_f = 0.5$, following Netzer & Marziani (2010), throughout the BLR. Putting Equation (22) in terms of N_c and recognizing that the Eddington luminosity is $L_{\rm Edd} = 4\pi GM_\bullet m_H c/\sigma_T$, Equation (22) becomes

$$\frac{dv_{\rm rad}}{dt} = \frac{GM_\bullet}{r^2}\left(\frac{\alpha_f L_{\rm AGN}}{\sigma_T N_c L_{\rm Edd}} - 1\right) = \frac{GM_\bullet}{r^2}(\Gamma F_M - 1) \tag{23}$$

after simplifying by introducing the Eddington ratio, $\Gamma = L_{\rm AGN}/L_{\rm Edd}$, and the force multiplier, $F_M = \alpha_f/\sigma_T N_c$, where σ_T is the Thomson cross section. It can now be easily seen that for $\Gamma F_M > 1$, the cloud is accelerated outward and accelerated inward when $\Gamma F_M < 1$ (Marconi et al. 2008; Netzer 2008; Netzer & Marziani 2010). The radii at which $\Gamma F_M = 1$ are when $N_c = 5.26\times 10^{22}$ cm^2 are indicated in Figure 5; for the $s = -1$ models at $r = 2.55\times 10^{17}$ cm, 7.12×10^{17} cm, and 5.84×10^{17} cm, and for $s = -2$, at $r = 8.16\times 10^{17}$ cm, 9.12×10^{17} cm, and 9.61×10^{17} cm for $p = 0$, 1, and 2, respectively.

If the BLR is created by a wind from the accretion disk (e.g., Elvis 2000), the gas clouds at $R_{\rm in}$ would have a velocity comparable to the escape velocity from the disk. Therefore, we assume the radial velocity at $R_{\rm in}$ to be the local escape velocity. Integrating Equation (23), we obtain

$$v_{\rm rad}(r)^2 = \frac{2GM_\bullet}{r}\left[\frac{\Gamma F_M}{2s/3 + 1}\left(\left(\frac{r}{R_{\rm in}}\right)^{2s/3+1} - 1\right) + 1\right], \tag{24}$$

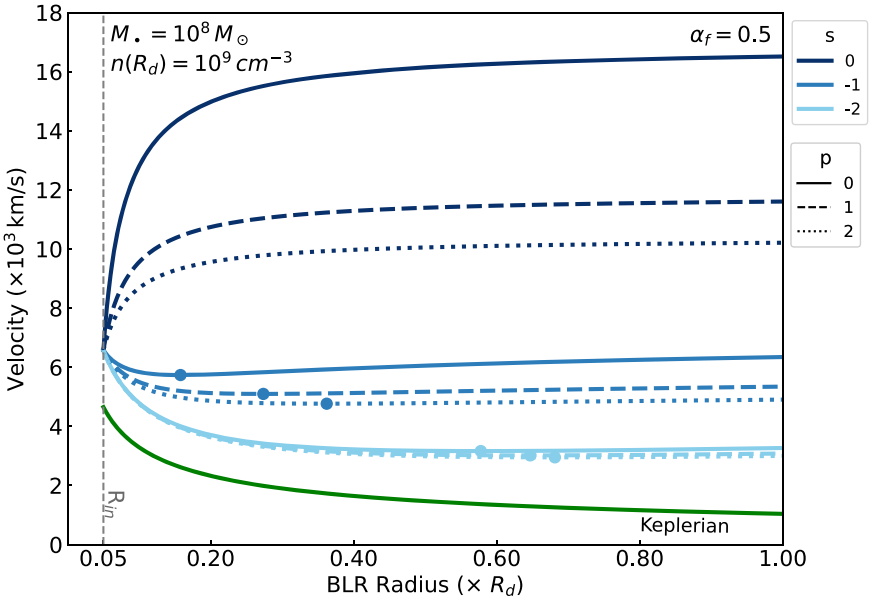

Figure 5. Rotational and radial velocities with respect to distance scaled to R_d. The escape velocity at $R_{\rm in}$ (dashed gray line) is 6578 km s^{-1}. The blue curves show the radial velocity given by Equation (24). The lighter the shade, the lower the s index. The solid, dashed, and dotted lines are $p = 0$, 1, and 2, respectively. The blue circles on the $s = -1$ and -2, $p = 0$, 1, and 2 curves mark the distance at which radiation pressure overcomes gravity and the clouds start accelerating outward. Each of these points corresponds to the critical $N_c = 5.26 \times 10^{22}$ cm^{-2}. When $s = 0$, the outward, radiation pressure force is greater than gravity at all distances. The green curve is the rotational velocity field, $v_{\rm Kep}$, described by Equation (19), which does not depends on the s and p indices.

the radial velocity field. Figure 5 shows $v_{\rm Kep}(r)$ and $v_{\rm rad}(r)$, Equations (19) and (24), respectively, for several values of the gas density and cloud radial distribution power-law indices.

The component of the radial velocity along the observer's LOS is given by

$$v_{\rm rad}^{||} = -v_{\rm rad}(r)(\cos\theta\cos i + \sin\theta\cos\phi\sin i). \quad (25)$$

Combining Equations (25) and (2), the delay-LOS velocity relation for a thin, spherical shell with radius r is a straight line in velocity and time delay space,

$$\tau = \frac{r}{c}\left(1 + \frac{v_{\rm rad}^{||}}{v_{\rm rad}}\right) \quad (26)$$

where the slope, $\frac{r}{c\, v_{\rm rad}}$, is positive for an outflow and negative for an inflow (Welsh & Horne 1991; Pérez et al. 1992).

3. Results

Here we present the velocity-resolved reverberation response functions (2DRFs) of, first, a spherical shell BLR with a radiation pressure driven outflow and, second, a rotating disk BLR, for their respective parameters listed in Table 2. We also present the velocity-integrated response functions (1DRFs), time-averaged line profiles, and rms line profiles.

To isolate the response amplitude, we subtract the initial BLR state (prior to the onset of the continuum pulse) from the response function at each τ. The 1DRF is normalized as $L(\tau)_{\rm norm} = \frac{L(\tau, v^{||}) - L_o}{L_{\rm max} - L_o}$, where L_o is the BLR luminosity in its initial state, and $L_{\rm max}$ is the peak luminosity of the BLR's response. We will present results from BLR models with both ICE and ACE. The BLR models presented here include $N_{\rm tot} = 10^5$ clouds, but as the BLR probably contains $\sim 10^6$ clouds (Arav et al. 1998; Dietrich et al. 1999), these can be considered a representative subsample.

Table 2
The Model Parameters for a Spherical and Disklike BLR

Parameter Description	Parameter Values	
Parameter	Sphere	Disk
Bulk motion	Radial	Keplerian
Half-angle width (σ)	90°	15°
Inclination (i)	...	0°–90°
Cloud initial gas density ($n(R_d)$)	10^9cm^{-3}	10^9cm^{-3}
Cloud distribution index (p)	0, 1, 2	0, 1, 2
Gas density index (s)	0, −1, −2	0, −1, −2

Note. Fixed values for all geometries are C_f=0.3, $L_{\rm AGN} = 10^{45}$ erg s^{-1}, $\Gamma = 0.07$, $\alpha_f = 0.5$, $Y_{\rm BLR} = 20$, $R_d \approx 10^{18}$ cm, and a representative subsample of 100,000 clouds.

3.1. Spherical BLR with Radial Outflow

In Figure 6 we show the 2DRF for an ICE BLR model that has a spherical geometry and a radiation pressure driven outflow, with gas density and cloud distributions $n(r) \propto r^{-1}$ and $N(r) = constant$ (defined by $s = -1$ and $p = 0$), respectively. The left panel shows the parabolic isodelay surfaces corresponding to the continuum pulse at various delays (Equation (2)) as it propagates through the BLR. The right panel shows the 2DRF, 1DRF, average line profile, and rms line profile. At $\tau = 0$, only clouds located along the LOS from the center of the BLR to the observer respond and these have the largest blueshifted velocities. The strongest changes in the line profile are shown by the rms profile, which is peaked and skewed to the blueshifted side of the line (far-right subpanel). The response remains entirely blueshifted until $\tau \geqslant 1/2Y_{\rm BLR} = 0.025$ (Equation (2) with $r = R_{\rm in}$, $\Theta = 90°$), when the response-front crosses into the far-side hemisphere. The response covers the greatest spread in LOS velocity at the light-crossing time of the inner radius, $\tau = 1/Y_{\rm BLR} = 0.05$ (bold curve in left panel), when it reaches the maximally redshifted LOS velocity. This

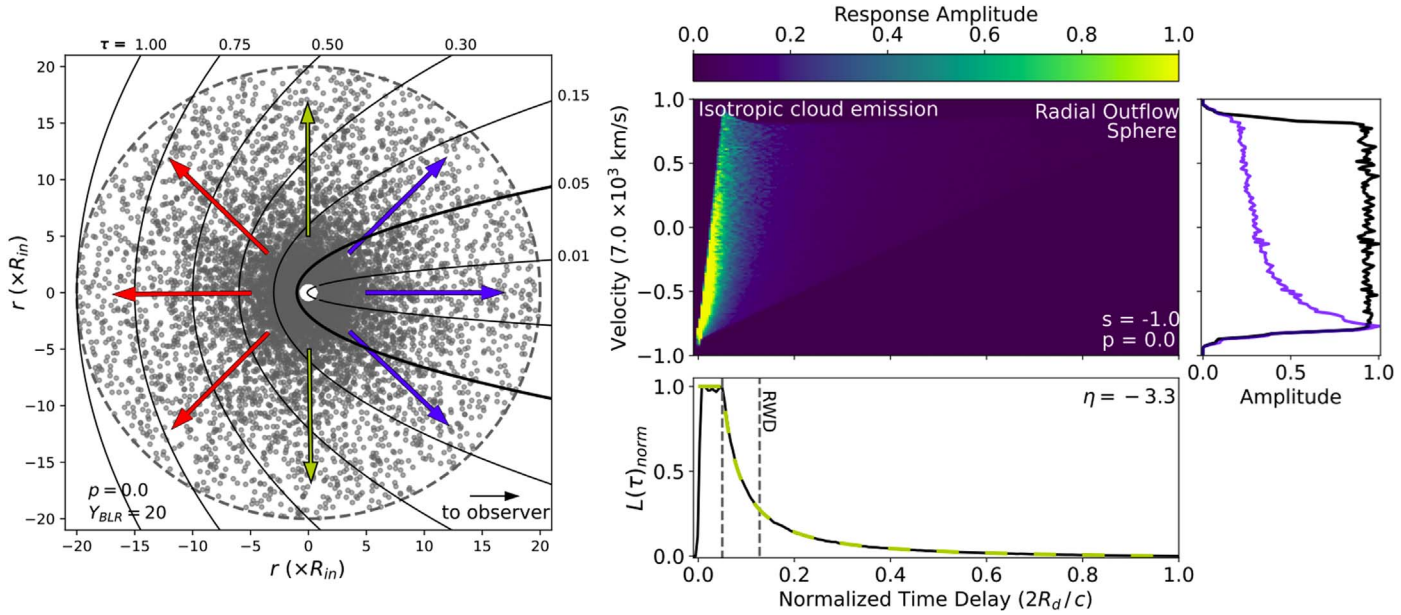

Figure 6. Left: cross section of a spherical BLR for $Y_{\rm BLR} = 20$ with isodelay surfaces overplotted for several values of the normalized time delay, τ. The arrows represent the velocity field, with blue, red, and yellow indicating a blueshift, redshift, and no shift, respectively. An animation of this Figure is also available. In the animation, the isodelay surfaces appear with τ from 0 to 1, which is denoted in the upper left-hand corner. In the static figure, all of the isodelay surfaces are shown, and each isodelay curve is labeled with it is corresponding value τ along the border. The bold isodelay curve corresponds to the light-crossing time of $R_{\rm in}$, $\tau = 0.05$. Right: response function for a spherical BLR with a radial outflow, for a gas density index $s = -1$ and cloud distribution index $p = 0$. All of the clouds in this BLR model are radiation-bounded. The color-scale represents the normalized response amplitude. The lower panel shows the velocity averaged, 1DRF in black, with the corresponding analytical model, calculated using Equation (14) with $\eta = -10/3$, in dashed yellow. In the animated version, the 1DRF is plotted in sync with the isodelay surfaces in the left panel. The dashed lines in the 1DRFs indicate the light-crossing time of $R_{\rm in}$, $\tau = 1/Y_{\rm BLR} = 0.05$, and the RWD =0.13. The right panel shows the time-averaged line profile (black) and the rms profile (blue). The animated version of this Figure also plots the line profile changing with τ (gray), which is in sync with the bottom panel and isodelay surfaces on the left. The profiles are each normalized to their respective maximum amplitude and binned to 100 km s^{-1} per bin.

(An animation of this figure is available.)

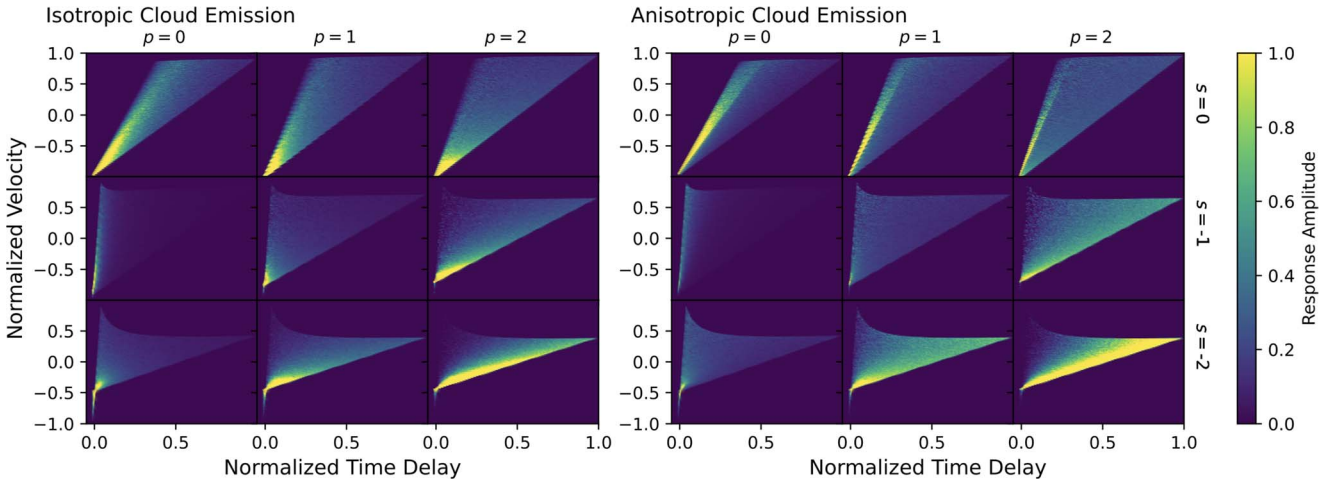

Figure 7. Velocity-resolved response functions (2DRFs) of spherical BLRs with radial outflow for varying s and p model parameters. The velocities are normalized to the maximum velocity of the respective BLR models. For instance, the response for $s = 0$, $p = 0$ is normalized to 17×10^3 km s^{-1} and for the $s = -2$, $p = 2$ model, to 7×10^3 km s^{-1}. Refer to Figure 5 for the maximum velocities in other cases.

also corresponds to the width of the flat-topped portion of the 1DRF (bottom-right subpanel). The response then narrows in velocity space as τ increases and becomes entirely redshifted for $\tau \geqslant 0.5$; the instantaneous line profiles are now red-asymmetric. After crossing the inner cavity, the response amplitude decays as τ increases until the BLR light-crossing time is reached ($\tau = 1.0$). It can be seen from Equation (14) that the relatively rapid decay is a consequence of the steeply declining emissivity distribution, where $\varepsilon_V \propto r^{-10/3}$ (Equation (12)), in this case. Although changes in the line profile begin in the blue wing then propagate redward as τ increases, the time-averaged line profile is symmetric, since in this ICE model there is an equal amount of line emission from the redshifted and blueshifted hemispheres of the BLR.

The 2DRFs of spherical shell BLR models, with $p = 0,\ 1,\ 2$ and $s = 0,\ -1,\ -2$ are shown in Figure 7 for both ICE and ACE cases. Their corresponding 1DRFs and delay-averaged line profiles are shown in the left and right panels of Figure 8,

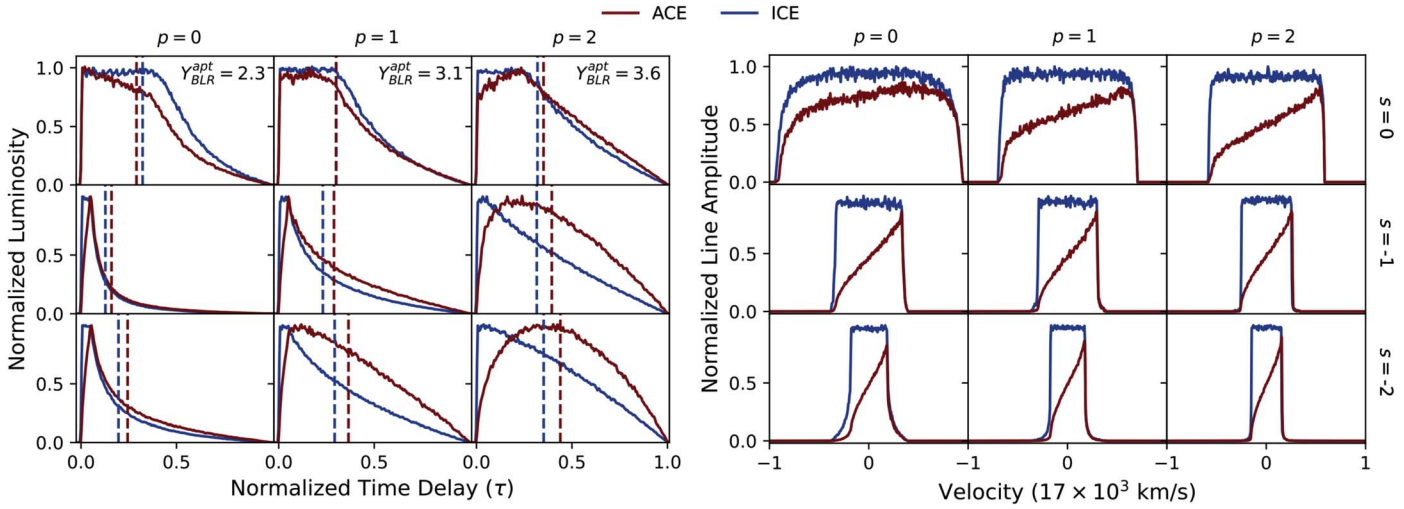

Figure 8. Left: the velocity-integrated 1DRFs for the models shown in Figure 7 for ICE (blue) and ACE (red) models. The dashed blue and red lines indicate the RWDs for the ICE and ACE models, respectively. The values of $Y_{\rm BLR}^{\rm apt}$ are given for each p when the ensemble includes matter-bounded clouds (see Section 3.1.1 for details). Right: the delay time integrated, line profiles of Figure 7. The profiles of ACE models (red) are normalized to the peak of the ICE model profiles. For each model, the velocities are normalized to the maximum velocity of the broadest line, which is when $s = 0$ and $p = 0$.

respectively. Considering first the ICE models with $s = -1$ and -2 (middle and bottom rows of Figures 7 and 8), it can be seen that as p increased from $p = 0$ to $p = 2$, the response narrows in velocity space, and its amplitude declines more gradually with increasing τ. For the larger values of p, the clouds with the highest velocities are located near $R_{\rm in}$ (see Figure 5) and make up a small fraction of the ensemble. These clouds, therefore, make a relatively small contribution to the response, which is dominated by clouds at larger radii, resulting in a response that is quite narrow in velocity space. The more gradual decline in the tail ($\tau > 1/Y_{\rm BLR}$) of the 1DRF is due to the more gradual decrease in emissivity with r, where for $s = -2$, $p = 0,\ 1,\ 2$, $\varepsilon_V \propto r^{-8/3}$, $r^{-5/3}$, and $r^{-2/3}$.

3.1.1. Matter-bounded Clouds

The 1DRFs of the ICE models in Figure 8 have a flat-topped portion at short delays, but the widths vary greatly between the $s = 0$ and $s = -1, -2$ models. This is because, for $s = 0$, the cloud size, R_{cl}, is constant and given that $n(R_d) = 10^9$ cm^{-3}, the innermost clouds are matter-bounded in the BLR's initial state, prior to the onset of the continuum pulse. These clouds do not respond to the increase in the ionizing flux (see Equation (10)). There is a transition from matter- to radiation-bounded clouds at the distance $R_{\rm MBC}$. Since $R_{\rm MBC} > R_{\rm in}$, the BLR responds as if it has a radial depth $Y_{\rm BLR}^{\rm mbc} = R_d/R_{\rm MBC}$, which is smaller than the true value, $Y_{\rm BLR}$. The transition radius varies with p and is listed in Table 3 along with the fraction of matter-bounded clouds during the initial state. Even a small matter-bounded cloud fraction corresponds to an $R_{\rm MBC}$ that is several times larger than the true $R_{\rm in}$. For example, when $p = 2$, only $\sim$1% of clouds are matter-bounded and do not respond, but $Y_{\rm BLR}^{\rm mbc} \approx 4$.

In addition to the clouds that are initially matter-bounded, there are clouds that are almost matter-bounded and become matter-bounded when the response-front reaches them. These clouds are at distances $r > R_{\rm MBC}$ and cause a turn-over feature in the response. That the clouds transition to the matter-bounded state further increases the apparent inner BLR radius to $R_{\rm MBC}^{\rm apt}$, which increases the width of the flat-topped portion of the 1DRF to $1/Y_{\rm BLR}^{\rm apt}$. For example, Figure 9 shows the 2DRF, 1DRF, and averaged line profile for a model in which 34% of clouds are initially matter-bounded, and 28% transition to matter-bounded (see Table 3, $s = 0$; $p = 0$). Overplotted on the 1DRF are two analytical 1DRFs calculated using Equations (15) and (16) with $Y_{\rm BLR}^{\rm mbc} = 2.60$, determined from the transition radius $R_{\rm MBC}$, and $Y_{\rm BLR}^{\rm apt} = 2.27$, which was determined using $R_{\rm MBC}^{\rm apt}$. Although these values are similar, the analytical curve for $Y_{\rm BLR}^{\rm apt} = 2.27$ is clearly a better match to the 1DRF. The values of $Y_{\rm BLR}^{\rm mbc}$ and $Y_{\rm BLR}^{\rm apt}$ for the other BLR models are listed in Table 3.

Table 3
Statistics for Matter-bounded Clouds (M.B.C.) in the $s = 0$ Models

p	% of M.B.C.	$R_{\rm MBC}/R_{\rm in}$	$Y_{\rm BLR}^{\rm mbc}$	Δ M.B.C.	$R_{\rm MBC}^{\rm apt}/R_{\rm in}$	$Y_{\rm BLR}^{\rm apt}$
0	34%	7.13	2.60	28%	10.5	2.27
1	7.51%	5.51	3.41	13%	7.78	3.07
2	1.35%	3.89	4.23	4%	6.48	3.65

Note. The first column is the cloud distribution index parameter p. The second through fourth columns are, respectively, the percentage of matter-bounded clouds, the distance at which the clouds are radiation-bounded, and scaled radial depth, $R_d/R_{\rm MBC}$, in the initial state. The fifth through seventh columns are, respectively, the percentage of initially radiation-bounded clouds that become matter-bounded, the greatest distance the bound state transition occurred, and the apparent scaled radial BLR size after the response completes. The true inner radius is 6.17×10^{16} cm and scaled size $Y_{\rm BLR} = 20$, for all BLR models presented here.

3.1.2. Anisotropic Cloud Emission

Figures 7 and 8 also show the 2DRFs, 1DRFs and τ-averaged line profiles for the ACE models, where ε_V also depends on *elf* and therefore becomes a function of θ, ϕ, and r. For ACE models in which all of the clouds are radiation-bounded, the observer sees <50% of the illuminated face for the clouds on the near side of the BLR. Therefore, at short time delays, the blue wings of the line profiles are suppressed, and the 1DRF is no longer flat-topped. The response peaks at delays when the observer sees the greatest number of clouds along an isodelay surface on the far side, where >50% of the

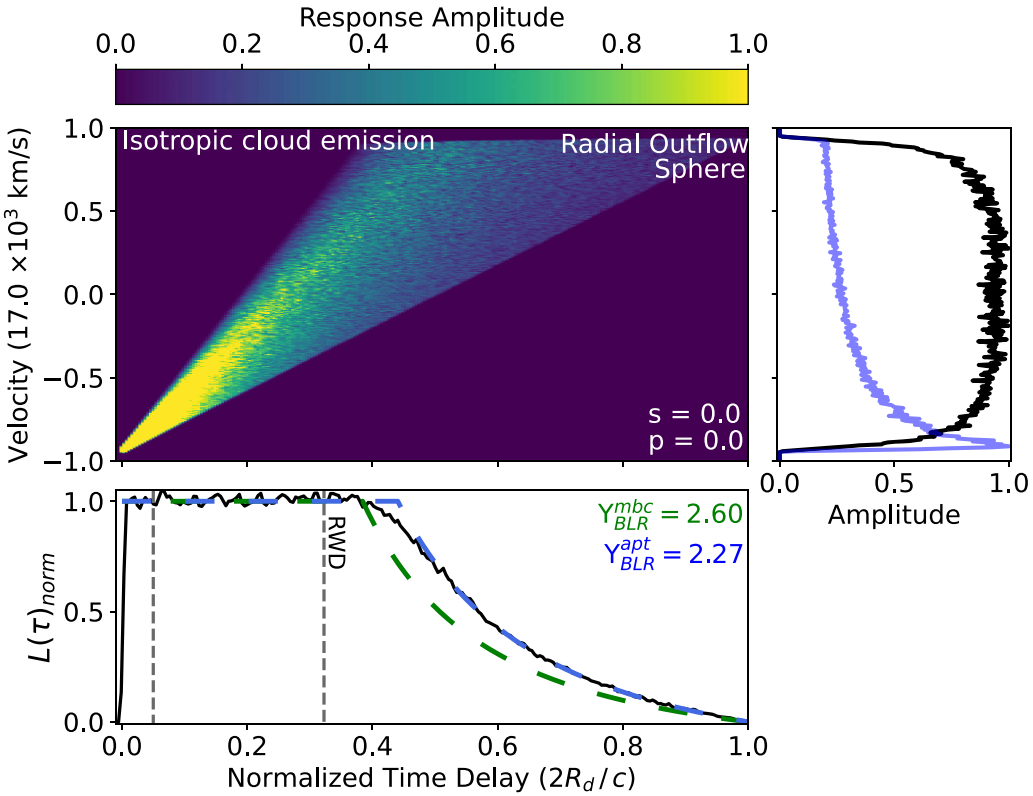

Figure 9. Same as the right panel in Figure 6, but with a gas density index $s = 0$, and therefore the ensemble includes matter-bounded clouds. The green and blue lines are the analytical 1DRFs for $Y_{\rm BLR}^{\rm mbc} = 2.60$ and $Y_{\rm BLR}^{\rm apt} = 2.27$, respectively.

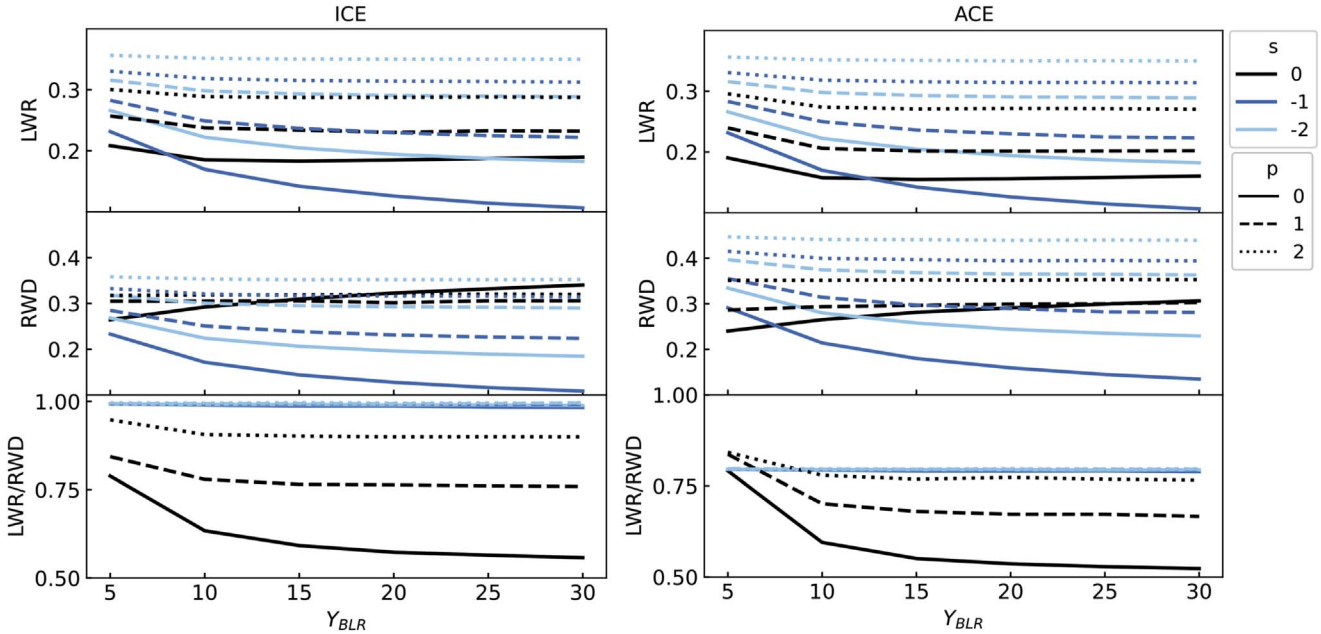

Figure 10. The LWR and RWD of the spherical ICE (left) and ACE (right) BLR models of varying $Y_{\rm BLR}$ for each combination of s and p parameters, with their ratio in the bottom panel. All of the models presented here with $s = 0$ contain matter-bounded clouds (see Section 3.1.1).

illuminated face is visible, are responding. This occurs when $\tau = 1/Y_{\rm BLR}$ for $p = 0$ and at later delays for models where the clouds are more uniformly distributed ($p > 0$). The τ-averaged line profiles of the ACE models are highly asymmetric and have half the amplitude of the corresponding ICE profiles. Clouds that are matter-bounded are assumed to emit isotropically and, therefore, have their *elf* values set to 1. The models that include matter-bounded clouds therefore have 1DRFs that are more similar to their ICE counterparts. In the line profiles, the asymmetry between the red and blue wings decreases as the fraction of matter-bounded clouds increases.

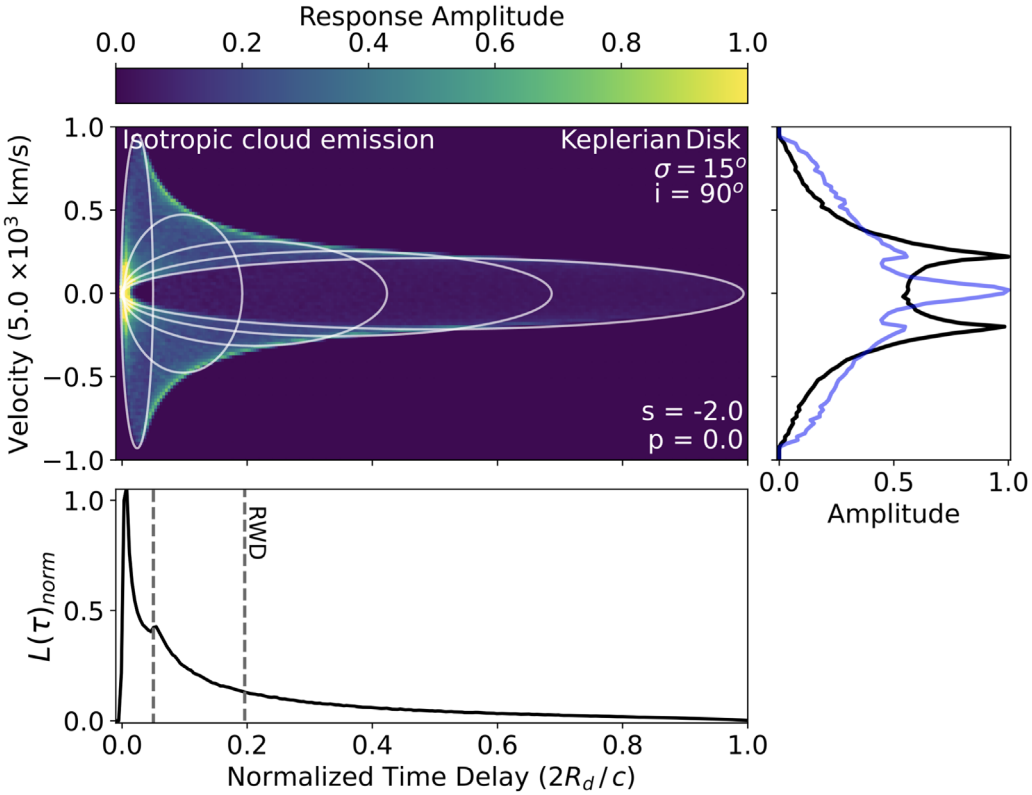

Figure 11. Same as the right panel in Figure 6, but for a disklike ($\sigma = 15°$) BLR with clouds moving in Keplerian orbits. The disk is viewed edge-on ($i = 90°$), $s = -2$, and $p = 0$. The dashed lines indicate the light-crossing time of $R_{\rm in}$, and the measured RWD =0.197. The white ellipses are defined by Equation (21). The system is entirely radiation-bounded clouds. An animated version of this Figure is available, and does not display the ellipses. In the animation, the 1DRF is plotted with τ from 0 to 1, along with the τ—varying line profile (gray). The changing line profile is a narrow, bright peak at $\tau = 0$, then quickly becomes lower in amplitude and broader with double peaks at the extremities of the profile's wings. These low-amplitude peaks slowly move back toward the center of the profile until $\tau = 1$. The τ—averaged line profile (black), rms (blue), and, in the animation, the τ—varying line profiles (gray) are normalized to their respective maxima.

(An animation of this figure is available.)

3.1.3. The Response-weighted Delay and Luminosity-weighted Radius

Figure 10 shows the variation with $Y_{\rm BLR}$ of the LWR, RWD, and the ratio LWR/RWD for ICE and ACE BLRs, and for each combination of s and p.

For ICE models with only radiation-bounded clouds, the LWR and RWD both decrease with increasing $Y_{\rm BLR}$, similar to the analytical relations shown in Figure 4, and the ratio LWR/RWD =1. Additionally, since LWR is not dependent on *elf*, the LWR values for the ICE and ACE models are identical. However, the response peaks at longer delays for ACE models, as discussed in Section 3.1.2, and thus the RWD is greater than for the corresponding ICE models. Therefore, for ACE models with radiation-bounded clouds, LWR/RWD ≈0.8 for all p and $Y_{\rm BLR}$ values.

For models with matter-bounded clouds, the RWD *increases* with $Y_{\rm BLR}$, due to these clouds not responding. The largest increase in RWD occurs for $s = 0$, $p = 0$, when about ∼30% of the cloud ensemble is matter-bounded. As a result, LWR/RWD decreases as $Y_{\rm BLR}$ increases, implying that the RWD overestimates the LWR and is dependent on the fraction of matter-bounded clouds and hence also $Y^{\rm apt}_{\rm BLR}$. The overestimation of LWR due to the presence of matter-bounded clouds ranges from a factor of ∼1.1 to nearly 2 for the ICE models. Furthermore, the LWRs for ACE models are slightly lower than those of the corresponding ICE models because the matter-bounded clouds have *elf*=1 (emit isotropically). The combined effect of ACE and matter-bounded clouds means the RWD overestimates the LWR by factors of ∼1.2 to ∼2.

3.2. Keplerian Disk BLR

Here we present the results of models in which the BLR is configured as a Keplerian disk. As specific examples, we discuss the reverberation responses for the ICE and ACE cases for an edge-on ($i = 90°$), rotating thin disk ($\sigma = 15°$), where the gas density decreases as r^{-2} ($s = -2$), U is constant, cloud size increases with distance, and the clouds are centrally concentrated. In this case, all of the clouds are radiation-bounded.

Figure 11 displays the 2DRF, 1DRF, time-averaged, and rms line profiles of the ICE model. For a specific orbital radius r, the projection of the isodelay surfaces and orbital velocities in the disk's plane is an ellipse in the 2DRF (Equation (21); Pérez et al. 1992). As can be seen in Figure 11, the characteristic rocket or bell-shaped 2DRF is created by the superposition of ellipses of varying r. Clouds at $R_{\rm in}$ have the largest LOS velocity range and respond at a shorter time delay than the clouds located at larger radii. The major axis of the corresponding ellipse is therefore aligned with the velocity axis. Conversely, the ellipse associated with the clouds at R_d, has the smallest velocity range and spans the largest range in time delay, and hence its major axis is aligned with the time delay axis. Rather than the flat top that was seen for the 1DRF of the spherical BLR, the disk 1DRF has a sharp peak at

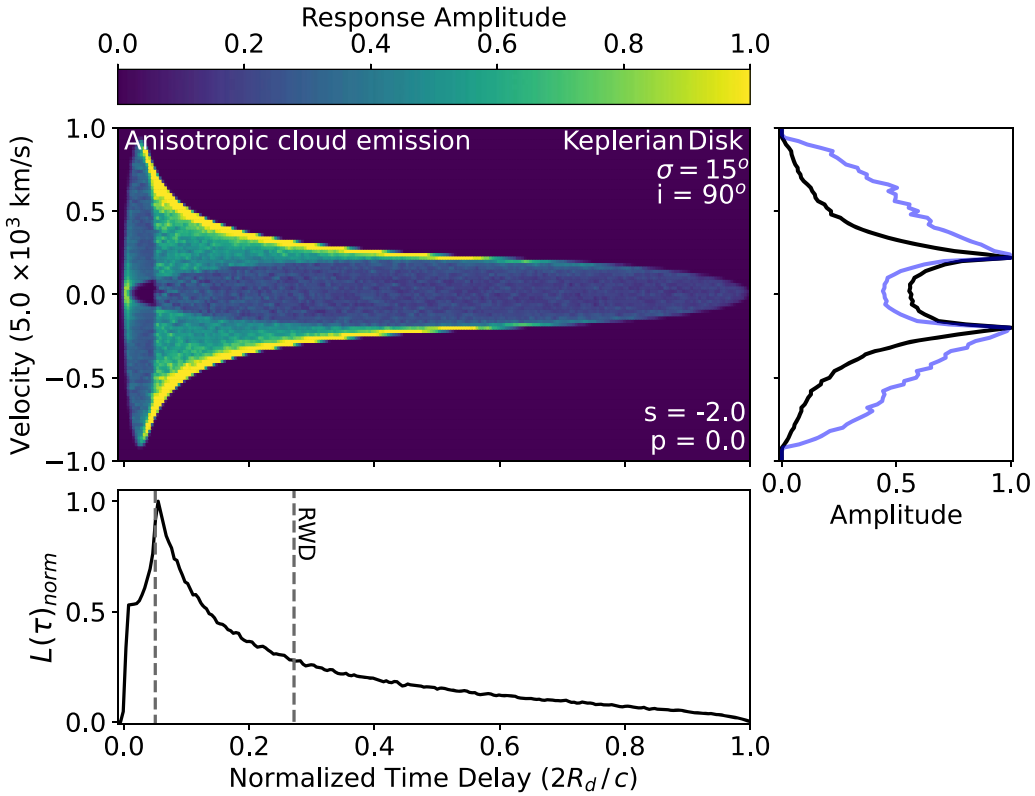

Figure 12. The same as Figure 11, including an animated version that is available, but for an ACE model. In the animation, the τ—varying line profile is a narrow, low-amplitude peak at $\tau = 0$, then quickly becomes brighter in amplitude and broader with double peaks at the extremities of the profile's wings. These high-amplitude peaks slowly move back toward the center of the profile until $\tau = 1$.

(An animation of this figure is available.)

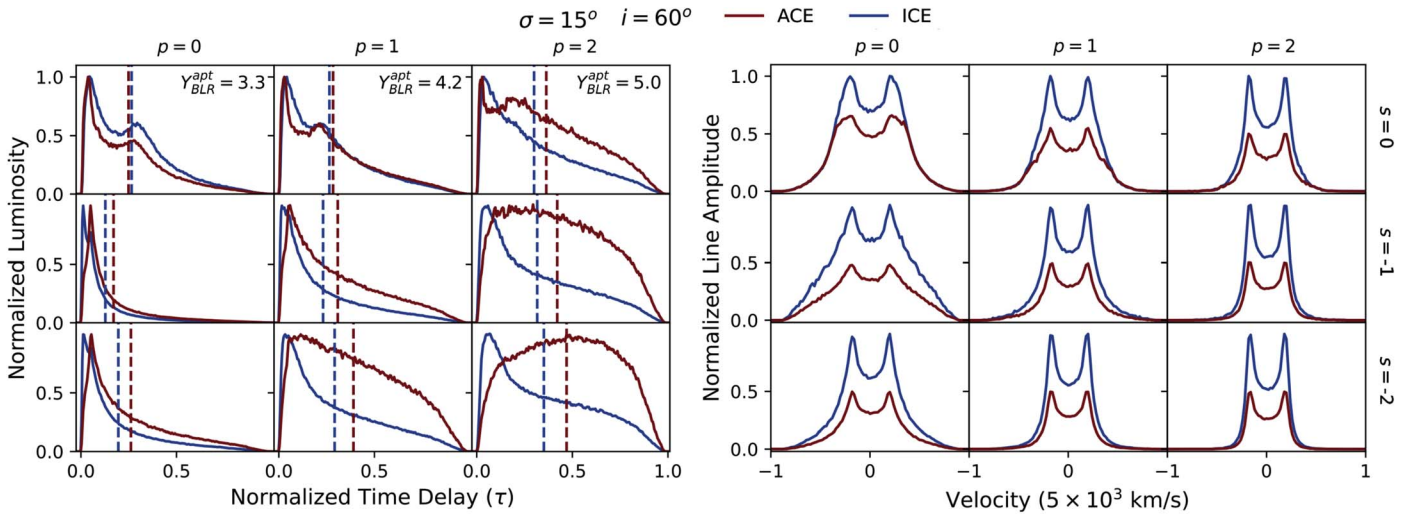

Figure 13. The same as Figure 8, but for disklike ($\sigma = 15°$) BLRs with clouds moving in Keplerian orbits and viewed from $i = 60°$.

$\tau = 0.0$, then a second, weaker peak in the response at the light-crossing time of the inner radius, $\tau = 0.05$, due to the decrease in the number of responding clouds while the response-front crosses the inner cavity. In this model, $\varepsilon_V \propto r^{-8/3}$, and as τ increases, more clouds at larger radii respond, and the tail of the 1DRF smoothly decreases until the light-crossing time of the BLR is reached ($\tau = 1$).

For an edge-on rotating disk, the τ—averaged line profile has distinctive, symmetrical redshifted and blueshifted peaks since the emission from the receding and approaching sides of the disk contributes equally. The response begins at $v_{\rm rot}^{\parallel} \approx 0$ km s^{-1}, and the amplitude is large enough that the rms profile has a central peak. The response then moves quickly and simultaneously to each wing, contributing to the weaker, symmetrical peaks in the rms profile.

The response of the corresponding ACE model is shown in Figure 12. The effect of ACE decreases the response amplitude during short time delays because the observer sees very little of the illuminated faces of the responding clouds. The initial response amplitude is approximately half that of the amplitude

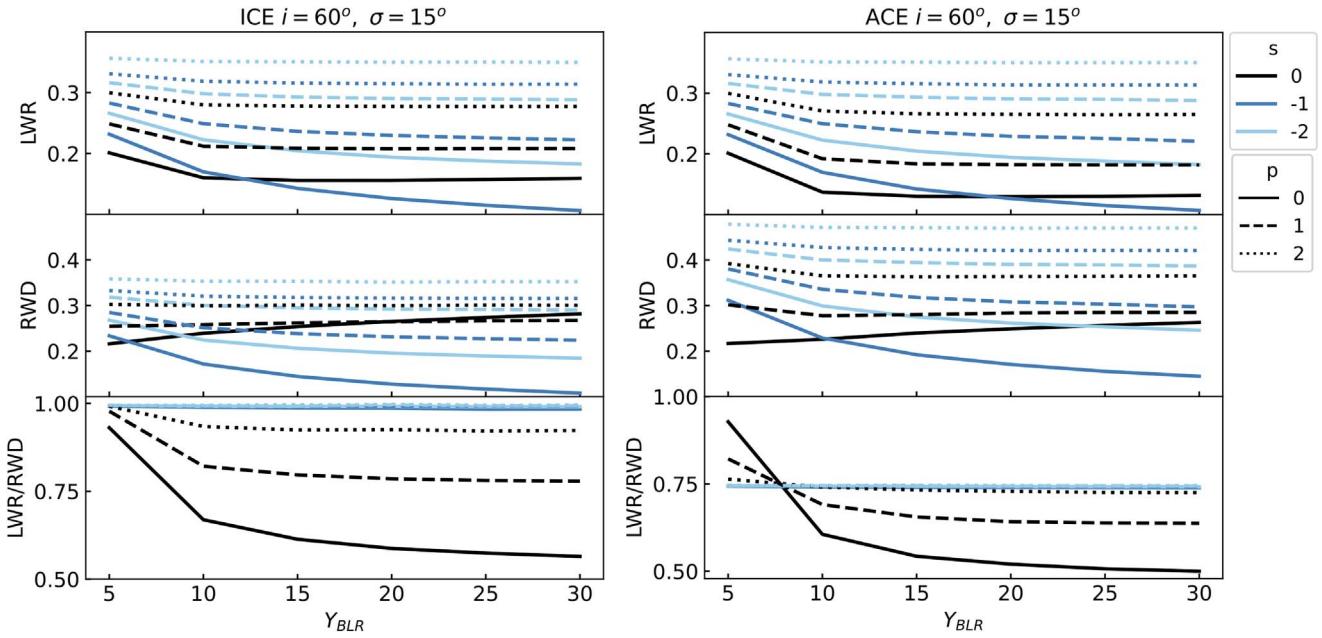

Figure 14. The same Figure 10, but for a rotating disk with $i = 60°$. All of the models with $s = 0$ contain matter-bounded clouds (see Section 3.2.2).

Table 4
Statistics for Matter-bounded Clouds (M.B.C.) for a Disk Geometry with $i = 60°$

p	% of M.B.C.	$R_{\rm MBC}/R_{\rm in}$	$Y_{\rm BLR}^{\rm mbc}$	Δ M.B.C.	$R_{\rm MBC}^{\rm apt}/R_{\rm in}$	$Y_{\rm BLR}^{\rm apt}$
0	22.87%	5.35	3.73	20%	7.46	3.3
1	3.72%	3.89	5.12	6.6%	5.67	4.2
2	0.43%	3.24	6.15	1.4%	4.70	5.0

in the ICE 1DRF model in Figure 11. Instead, in the ACE model, the response peaks at $\tau = 0.05$, when the observer receives the response from the clouds with $elf > 0.5$. For the same reason, although the response begins in the core of the line profile, the effect of ACE decreases the response amplitude, and the rms profile does not have a central peak.

Figure 13 shows the 1DRFs and line profiles for disk models inclined at $i = 60°$ with varying values of the s and p parameters for both ICE and ACE cases. We chose to present the $i = 60°$ BLR models, since an edge-on BLR would be obscured to an observer by the surrounding dusty torus. However, we still want to present a high inclined disk to show distinctly separated peaks in the line profiles. Other choices of intermediate inclinations produce qualitatively similar results. For ICE models where all of the clouds are radiation-bounded, the general behavior of the 1DRFs depending on s and p are similar to the spherical models. In the ACE models, the clouds on the far side relative to an observer contribute more emission to the total response, so the peak response occurs at longer time delays as p increases. When clouds are concentrated near $R_{\rm in}$ (i.e., $p = 0$), the peak is at $\tau = 1/Y_{\rm BLR}$.

Both the ICE and ACE models have symmetrical line profiles with redshifted and blueshifted peaks, characteristic of rotating disks. Since the *elf* is symmetrical about the disk axis, the ICE and ACE line profiles have the same shape, but the ACE model profiles have half the amplitude.

When $s = 0$, the presence of matter-bounded clouds causes both peaks in the 1DRF to be broader, and the second peak occurs at $\tau \approx 1/Y_{\rm BLR}^{\rm apt}$ rather than $\tau = 1/Y_{\rm BLR}$. The percentages of matter-bounded clouds, $R_{\rm MBC}$, and $Y_{\rm BLR}^{\rm apt}$ for each model are listed in Table 4. Since *elf*=1 (isotropic emission) for matter-bounded clouds, the amplitudes of the ACE line profiles approach those of the ICE models as the fraction of matter-bounded clouds increases (see Table 4).

The LWRs and RWDs for a disk with $i = 60°$, Figure 14, show the same general trends with $Y_{\rm BLR}$ as the spherical BLR. In particular, the ICE models (left panel) and the corresponding spherical BLR models (left panel in Figure 10) show very similar behavior. However, the RWDs for the ACE models are longer for a disk than a sphere, and therefore the LWR/RWD ratio has slightly lower values (LWR/RWD =0.75, for $s \neq 0$). When models have matter-bounded clouds, LWR/RWD <1 for both ICE and ACE models, and the ratio decreases as the fraction of matter-bounded clouds increases ($p = 2 \rightarrow 0$) and as $Y_{\rm BLR}$ increases. Further discussion of the effects of matter-bounded clouds is given in Section 3.2.2.

3.2.1. Effects of Inclination

Cross-sectional diagrams of disklike BLR ensembles at $i = 0°$, 45°, and 90° with isodelay surfaces overplotted are shown in Figure 15. The effects of inclination on the 1DRFs and line profiles are shown in Figure 16 for both ICE and ACE models with $s = -2$ and varying p. When the disk is face-on to the observer, the 1DRF is zero until $\tau = 0.03$, when the response-front reaches the clouds at the inner radius. As i increases, the response begins at progressively shorter delays until, at $i = 90° - \sigma$ the response begins at $\tau = 0$. Additionally for ICE models, the 1DRF peak becomes narrower and the tail overall extends to longer delays, as i increases. At larger inclinations, the ACE 1DRFs show much stronger, extended responses at longer delays than their ICE counterparts.

When the disk is face-on, there is a sudden decrease in the 1DRF at $\tau = 0.37$. The inflection point corresponds to the delay, $\tau = \frac{1}{2}(1 - \cos(90° - \sigma))$, when the isodelay surface intersects with the outermost edge of the disk surface facing the

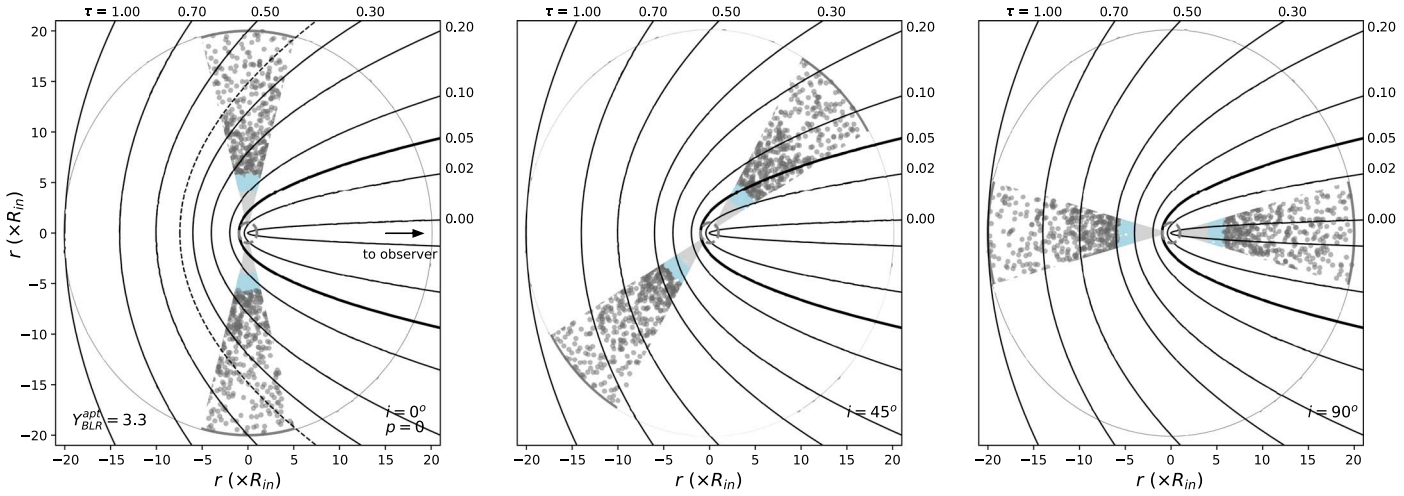

Figure 15. Isodelay surfaces overplotted for a disklike, $\sigma = 15°$, BLR viewed from left to right at, $i = 0°$, $i = 45°$, and $i = 90°$. The isodelay surfaces are labeled with the corresponding delays, τ, across the top and down the right-hand side of each subfigure. The light gray points are matter-bounded clouds, which do not respond. The light-blue points represent clouds becoming matter-bounded when the continuum pulse reaches them, and the gray clouds are always radiation-bounded. The dashed line in the $i = 0°$ panel is the isodelay surface corresponding to inflection point seen in the response in the left panel of Figure 16. The isodelay curve in bold is the light-crossing time for $R_{\rm in}$.

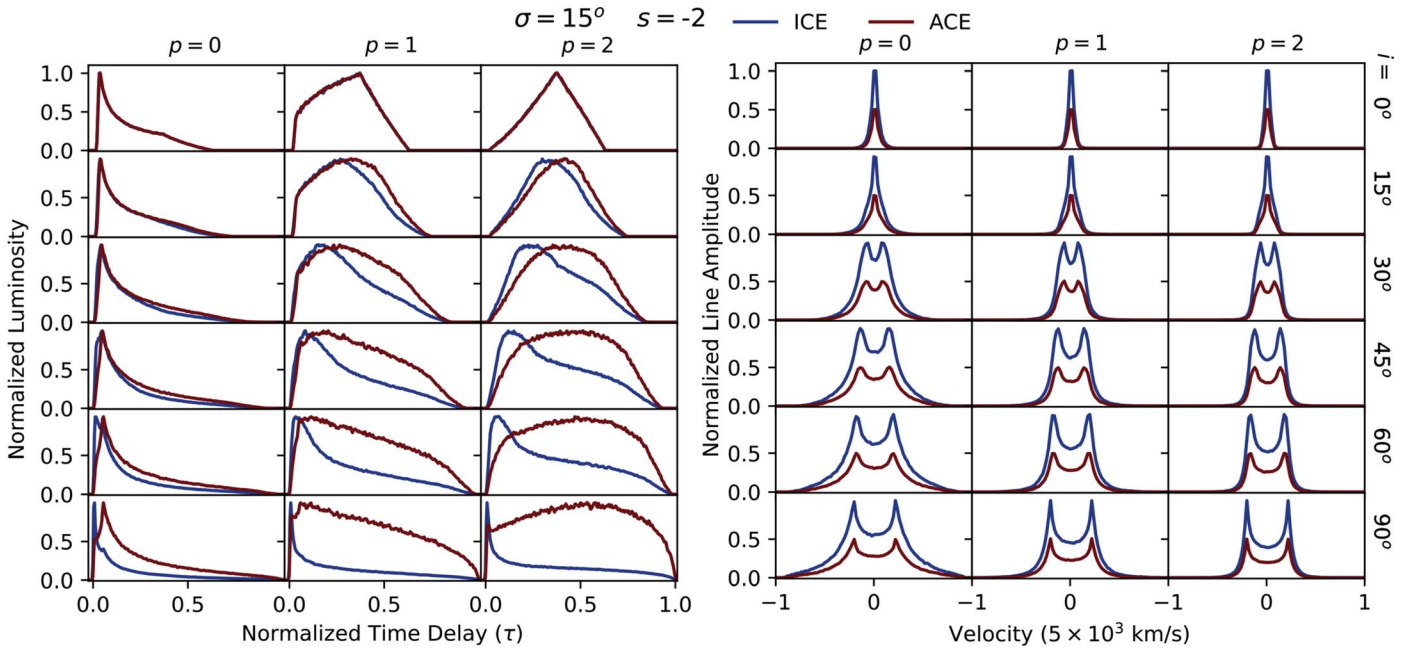

Figure 16. 1DTFs (left) and line profiles (right) for a disklike ($\sigma = 15°$) BLR with clouds moving in Keplerian orbits and viewed from face-on to edge-on, $i = 0°$, 45°, 90°, for each row and increasing $p = 0$, 1, 2 for columns left to right, and $s = -2$.

observer, shown in Figure 15 as a dashed line. The 1DRF peaks at this τ-inflection point when $p = 1$ and 2, as the largest number of clouds are responding at this delay. The response is complete at $\tau = \frac{1}{2}(1 - \cos(90° + \sigma))$.

The right panel of Figure 16 shows the line profiles for the same models, where the profile amplitudes have been normalized to the maximum amplitude for the ICE model. With respect to the line center, the peaks are located at $\pm \sin i\ v_{\rm min}/v_{\rm max}$; therefore, the gap between them is zero at $i = 0°$ resulting in a single-peaked profile (Robinson 1995). Otherwise, when the disk is inclined, the line profile shape has the characteristic, symmetrical peaks about the center of the profile. The trough between the peaks also gets deeper with increasing i and p.

3.2.2. Models with Matter-bounded Clouds

Figure 17 is the same as Figure 16, but for models with $s = 0$. Here, clouds within $R_{\rm MBC}$ are matter-bounded and do not respond. This creates an "apparent" inner cavity in the BLR that is larger than $R_{\rm in}$. Therefore, the response has a delayed start that is dependent on $R^{\rm apt}_{\rm MBC}$, in addition to its dependence on i and σ, as discussed above. However, as $R_{\rm MBC} < R_d$, this does not affect the clouds at the largest radii in the BLR, and the response ends at the same delay, $\tau = \frac{1}{2}(1 - \cos(90° + i + \sigma))$, regardless or whether or not matter-bounded clouds are present. The 1DRFs are double-peaked at $i \geqslant 30°$, where each peak represents the response-front encountering the near side then far side clouds at $R_{\rm MBC}$. The time delay between the two peaks lengthens as

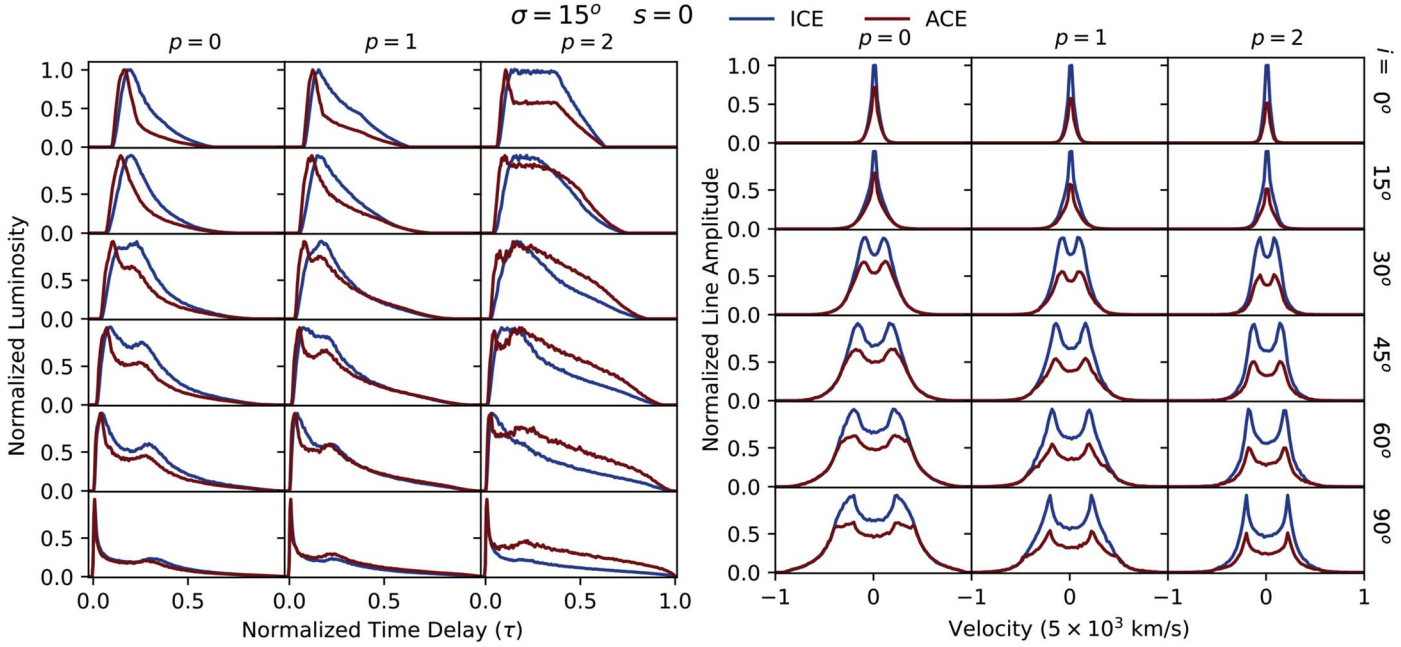

Figure 17. The same as Figure 16, but with matter-bounded clouds in the ensemble ($s = 0$).

i increases, since the second peak occurs at $\tau = (2Y_{\rm BLR}^{\rm mbc})^{-1}(1 - \cos(90° - i))$ and also as p decreases due to the increase in the fraction of matter-bounded clouds.

In general, the ICE and ACE line profiles in the right panel of Figure 17 have a similar shape. However, the presence of matter-bounded clouds creates shoulder-like features in the line profiles of ACE BLR models when $i \geqslant 60°$. This can most clearly be seen for the model with $i = 90°$ and $p = 0$. The symmetrical inflections are a result of matter-bounded clouds within $R_{\rm MBC}$ emitting isotropically, then, as the isodelay surface propagates throughout the BLR, radiation-bounded clouds at larger radii respond and emit anisotropically. The width of these shoulders relates to $R_{\rm MBC}$ and thus increases as p increases. The width of the shoulders broadens with increasing p and become more smoothed with decreasing i; therefore, we do not clearly see these features for $p > 1$ and $i \leqslant 45°$.

4. Discussion

We have presented a new BLR reverberation mapping forward-modeling code, BELMAC, that incorporates various velocity field models to calculate the velocity-resolved response. We assume the clouds are bound spheres, which follows similar modeling work such as Robinson & Perez (1990), Netzer (2008), Marconi et al. (2009), Goad et al. (2012), and Lawther et al. (2018). The version of the code used here assumes hydrogen recombination to determine cloud luminosity, where the clouds can optionally emit isotropically (ICE) or anisotropically (ACE). We presented BLR cloud ensemble models with a radiation pressure driven outflow in a sphere and Keplerian orbits in a disk, respectively.

BELMAC does not provide a full hydrodynamic treatment of the gas flows and does not consider intercloud radiative transfer. However, representing the BLR as a cloud ensemble offers the ability to quickly and efficiently explore multiple configurations of BLR geometries and velocity fields. This representation may impose some limits on BELMAC's predictions.

4.1. The Radiation Pressure Driven Flow

The BLR clouds are photoionized and therefore subjected to radiation pressure forces due to scattering and absorption. Disregarding radiation pressure could lead to significant underestimations or overestimations of $M_\bullet$ as determined by the virial method (see, e.g., Marconi et al. 2008; Netzer & Marziani 2010). Although Keplerian motion was found to dominate the BLR velocity field in the AGN discussed in Section 1.2, there may also be weak radial flows. In fact, there is evidence for inflows in NGC 3783 (Amorim et al. 2021a). Furthermore, these AGNs have low to moderate Eddington ratios ($\Gamma < 0.2$, based on the reported $L_{\rm AGN}$ and $M_\bullet$), but outflows are expected to be much stronger in high and super-Eddington AGNs. The outflows may be associated with a disk wind, with the relative prominence of the disk and wind components scaling with AGN luminosity (Elitzur et al. 2014). This suggests that the dominant emission-line-producing structures in the BLR are dependent on the SMBH's accretion rate.

In our adopted model (Equation (23)), there is an outflow when $\Gamma F_M > 1$ where $F_M \propto 1/N_c$; therefore, the conditions for an outflow in our models depend on the Eddington ratio, Γ, and column density. Since Γ is dependent on $L_{\rm AGN}$ and $M_\bullet$, it will be an output when BELMAC is applied to model real data, but here we have fixed the AGN values to $\Gamma = 0.07$ and $M_\bullet = 10^8\ M_\odot$. To achieve an outflow, the clouds must have $N_c < 5.26 \times 10^{22}$ cm^{-2} (see Equation (23)). For models with $s = 0$, clouds have a constant cross-sectional area and $N_c(r) \sim 10^{22}$ cm^{-2}; thus, $\Gamma F_M > 1$ throughout the entire BLR. When cloud cross-sectional areas vary with distance ($s \neq 0$), the clouds with $N_c(r) > 5.26 \times 10^{22}$ cm^{-2} are too massive for radiative forces to overcome gravity. As $N_c(r)$ decreases, the F_M increases, because the clouds expand to maintain constant mass.

The above density calculations are also dependent on the initially defined gas density, $n(R_d)$. If $n(R_d)$ is large, e.g., $n(R_d) = 10^{10}$ cm^{-3}, $\Gamma F_M < 1$ throughout the BLR and

$v_{\rm rad}(r) \rightarrow \sqrt{GM_{\bullet}/r}$. Furthermore, in these models we have assumed that the mass of the clouds is conserved (i.e., $m_{cl}(r) =$ constant). In real BLRs, the relation between the sizes of clouds and their masses may vary, leading to a more complex gas density distribution. Varying the cloud mass would alter our adopted radial cloud motion model and could produce less-boxy line profiles. The last parameter to consider is α_f, the fraction of $L_{\rm AGN}$ absorbed by a cloud. A more realistic BLR model would let α_f depend on the ionization parameter and N_c, but here we have opted to keep that quantity constant ($\alpha_f = 0.5$; Equation (22)).

The line profiles produced by the spherical shell-radial flow models tend to be boxy, unlike the observed broad-line profiles in most AGNs, which typically resemble a Gaussian or Lorentzian profile. This is a feature of the radial velocity field model adopted here. As can be seen in Figure 5, the radial velocity curves rapidly level off to a terminal velocity, within $\sim$0.1–0.3 R_d. As $v(r) =$ constant in the outer regions, the dispersion in LOS velocity varies little with radius, resulting in flat-topped profiles. Although, varying $\alpha_f(r, t')$ could reduce the acceleration so that the terminal velocity is reduced at a larger radius. Here, the velocity range for the large majority of clouds in the ensemble is quite small, resulting in boxy line profiles that do not resemble most observed broad emission lines. For $s = 0$ and $p = 0$, the clouds experiencing the greatest acceleration are also matter-bounded clouds, which do not contribute to the reverberation response, but still contribute to the average line profile. Additionally, allowing the cloud mass to vary, such as varying cloud mass, could produce less-boxy profiles. Finally, a BLR model with combined velocity fields, with nonradial components contributing to the LOS the velocity (such as turbulence and/or Keplerian motion) will tend to produce more Gaussian or Lorentz-like line profiles that would be more representative of observed BELs.

4.2. Representation of Real Broad Emission Line Responses

Utilizing simple recombination theory (Equation (10)) for the cloud luminosity is a reasonably good approximation for Hα emission. Roughly speaking, the Hα flux emitted per unit area by a given cloud is proportional to the column density of ionized gas, $N_s(r)$. This in turn depends on $U(r, t')$ and therefore responds to a changing ionizing radiation field. We can also make general statements about the emissivity distribution for other broad lines. For instance, the high-ionization emission lines, such as CIV $\lambda\lambda$ 1551, 1548 Å, are mainly emitted near $R_{\rm in}$ where the ionizing radiation field is strongest (Osterbrock & Mathews 1986). The response of CIV would peak at a short time delay, then rapidly drop off with time delay. Therefore, we'd expect the response behavior of high-ionization lines like CIV to be somewhat similar to models with small values of s and p. Conversely, low-ionization lines, such as MgII $\lambda\lambda$ 2795, 2803 Å, have an emissivity distribution that varies more slowly with radius and so can be approximated by specifying larger s and p values. The power-law approximation of $\varepsilon(r)$, which includes the s and p parameters, should provide a general guide to the dependence of a given line's reverberation response to $U(r, t')$, $n(r)$, and $N_c(r)$. However, the emissivity distributions for true emission lines in BLRs are certainly more complex functions than implied by Equation (12).

When the *elf* is used (Equation (11)), it provides a reasonable approximation for anisotropic line emission from a distribution of clouds, and the ACE models should be generally representative of emission lines that are optically thick. For example, ACE models can be utilized to approximate the response of Lyα that is emitted in the ionized part of the cloud and escapes almost entirely through the illuminated face, but has a very low probability of escaping through the nonilluminated face. ICE models represent lines that are optically thin, such as CIV, which can escape isotropically if the cloud contains no dust. Furthermore, we assume that a matter-bounded cloud also becomes effectively optically thin, allowing the line emission to escape isotropically. We could expect dust to survive in the partially ionized and neutral interiors of BLR clouds (Baskin & Laor 2018). Dust is not explicitly included in the current version of BELMAC, but ACE, modeled with the *elf* parameter, could also be used to approximate the effects of dust extinction in BLR clouds.

4.3. Inferring Black Hole Mass from the Reverberation Lag

As discussed in Section 1 an important motivation for BLR reverberation mapping is to determine $R_{\rm BLR}$ and hence $M_{\bullet}$ via the virial theorem (Equation (1)). The BLR models presented Section 3 show that the RWD is not always equivalent to the LWR. Matter-bounded and anisotropically emitting clouds have a significant affect on the response-weighted lag, $t'_{\rm RW}$, which could lead to overestimates of the SMBH mass. If we assume the velocity dispersion is determined exactly and assume $ct'_{\rm RW} = R_{\rm LW} = R_{\rm BLR}$ ($2R_{\rm d}{\rm LWR} = R_{\rm LW}$; see Section 1.2) then,

$$\frac{M_{\bullet}}{fM_{\bullet,\rm vir}} = \frac{\rm LWR}{\rm RWD} \tag{27}$$

where $M_{\bullet}$ is the true black hole mass and $M_{\bullet,\rm vir}$ is the mass inferred from reverberation mapping. Since we are assuming $2R_{\rm d}{\rm LWR} = R_{\rm BLR}$, if LWR/RWD <1, then RWD is overestimating LWR and therefore also $M_{\bullet}$. This is the case for all of the models with matter-bounded clouds and/or ACE presented in Figures 10 and 14.

Figure 18 shows the LWRs and RWDs for the spherical and disk BLR models that include matter-bounded clouds from Figures 10 and 14. The bottom panels show the RWD can be $\sim 1.1 \times$ LWR, for the smallest BLRs, to nearly $2 \times$ LWR for $Y_{\rm BLR} \gtrsim 20$. ACE also results in LWR/RWD <1, even when 100% of the clouds are radiation-bounded. Figures 10 and 14 show that RWD $\approx 1.2 - 1.5 \times$ LWR for ACE models with no matter-bounded clouds. As discussed above, ACE is a fair representation of optically thick emission lines and the possible extinction by dust embedded in the cooler regions of the clouds. Therefore, in the sample of BLR models explored here, $R_{\rm BLR}$ is correctly determined from $t_{\rm RW}$ only when all of the clouds in the BLR ensemble are radiation-bounded *and* emitting isotropically. Given the conditions in real BLR stated in Section 4.2, this scenario is unlikely to occur for Balmer lines, which tend to be optically thick (Osterbrock & Mathews 1986). The LWR/RWD results shown in Figure 18 of ACE models are reasonable predictions for reverberation responses with similar BLR properties.

The influence of matter-bounded clouds on the LWR/RWD ratio is more model dependent than the effect due to ACE. Since matter-bounded clouds occur when the Strömgren depth is equal to or exceeds the cloud size, their presence depends on U and n, as well as the cloud size. Furthermore, the fraction of matter-bounded clouds within the model depends on the radial

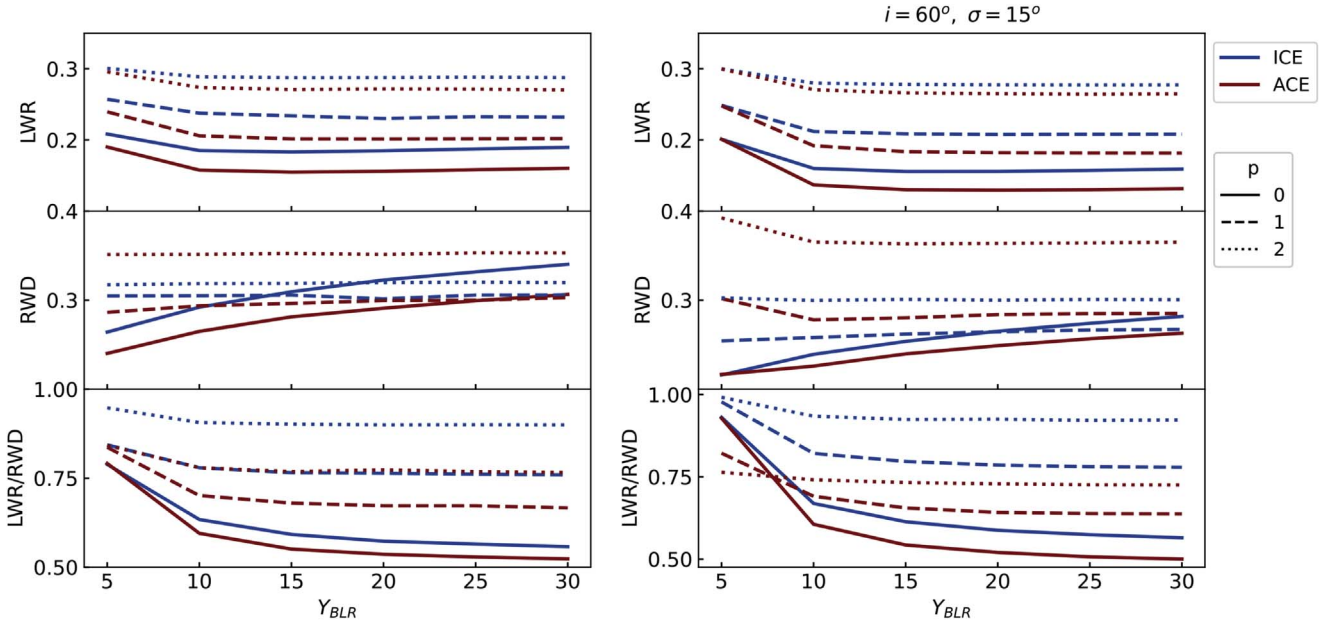

Figure 18. The LWR, RWD, and LWR/RWD for (left) spherical and (right) disklike ($\sigma = 15°,\ i = 60°$) BLR models, but for only models containing matter-bounded clouds ($s = 0$). The blue and red lines represent ICE and ACE BLR models, respectively.

cloud distribution. For these reasons, it is unclear how important their effect on LWR/RWD would be in real BLRs. However, our results suggest that even if only ∼1% of the clouds are matter-bounded, they can significantly affect the LWR/RWD. Therefore, the results shown in Figure 18 suggest the lag measured from cross-correlation analysis may not relate to $R_{\rm BLR}$ as straightforwardly as previously assumed. In forthcoming work, we will revisit this issue with the next version of BELMAC that implements photoionization models.

4.4. Comparison to TORMAC

Although TORMAC was designed to simulate reverberation of the torus dust emission in AGNs, it is worth discussing similarities and differences between TORMAC and BELMAC.

TORMAC includes physics potentially important for both the torus and the BLR: cloud occultation, cloud shadowing, and the effect of cloud orientation. A cloud is occulted and its emission is attenuated when another cloud is positioned along the LOS between the former cloud and the observer. The strength of the attenuation depends on the number of occulting clouds and their optical depths. Cloud shadowing occurs when a cloud is positioned within the shadow of another cloud intervening between it and the illuminating source. A cloud without direct exposure to the source is indirectly heated by the diffuse emission from neighboring clouds and emits isotropically (Almeyda et al. 2017, 2020). As a general point, we expect cloud occultation and shadowing to be less important for the BLR's gas clouds, even if the clouds themselves are optically thick for a given line, because the BLR as a whole is presumed to be optically thin (i.e., $C_f < 1$). Therefore, these two effects are not included in the current version of BELMAC, but could be incorporated in later versions. Cloud emission anisotropy, on the other hand, is expected to be important in some situations and is incorporated in BELMAC via the *elf* parameter (Equation (11)). This is based on the orientation-dependent fraction of the cloud's illuminated surface that is viewed by the observer. TORMAC includes a more sophisticated implementation of cloud orientation effects than BELMAC's *elf* parameter. The anisotropic emission of a cloud in TORMAC, adopted from the clumpy torus model by Nenkova et al. (2008a), is wavelength dependent. In this model, the spectrum of a cloud is approximated by averaging over the emission from many slabs of gas at varying orientation angles relative to the central illuminating source (Almeyda et al. 2017, 2020).

TORMAC also includes anisotropic illumination of the torus. Edge darkening of the AGN's accretion disk causes the illuminating radiation field to be anisotropic. As a result, the dust sublimation radius is not constant, but a function of polar angle and the dust can exist closer to the source near the midplane than toward the pole. For dust clouds arranged in a sphere and anisotropically illuminated, the cross section of the inner dust-free cavity would have a figure-eight shape (Almeyda et al. 2017; Baskin & Laor 2018; Kudoh et al. 2023). Although we do not explore anisotropic illumination here, it is included in BELMAC. For the BLR, this effect will result in both the ionization parameter (Equation (9)) and the outer boundary, the dust sublimation radius, becoming functions of polar angle, θ.

4.5. Future Development of BELMAC

The forthcoming versions of BELMAC will include several new capabilities. These include the following:

1. introduction of photoionization model grids to calculate the reverberation responses in several different BELs;
2. Procurement of the absorbed ionizing flux fraction (α_f) from the photoionization model grids;
3. The ability to include more complex combinations of geometries and velocity fields; and
4. A parameter estimation procedure that uses BELMAC to model BLR reverberation mapping data.

In the next version of BELMAC, the line emission of each individual cloud will be calculated by interpolating in a

precomputed grid of photoionization models. This will provide a more sophisticated calculation of the Hα (and Hβ) flux and will enable modeling of the responses of other lines (e.g., Lyα, CIV λ1550, and Mg λ2800), for which the simple recombination treatment used here is not applicable. The photoionization grids can be computed with CLOUDY (Ferland et al. 2017) or a similar photoionization code and will span ranges in U, n, and N_c sufficient to cover the variations of these cloud properties with r and also, in the case of U, with t'. Values of $\alpha_f(r, t')$, which is used to determine the force multiplier for the radiation pressure force (see Section 2.5.2, Equation (24)), will also be obtained from the photoionization grids.

Currently, BELMAC is capable of combining velocity fields, such as rotational motion with random turbulence, or rotational and radial motion for noncircular cloud orbits, in either spherical shell or disk geometries. A bicone geometry will be added to simulate responses for bipolar winds. Therefore, by combining geometrical components, BELMAC will be able to model disk-wind BLRs, which have been discussed by many authors (e.g., Waters et al. 2016; Elvis 2017; Yong et al. 2017; Matthews et al. 2020, and references therein). An exploration of multi-emission-line responses for combined velocities and geometries will be presented in a forthcoming paper. However, an example of this capability was recently presented in Bentz et al. (2023), where BELMAC was used to model Hβ reverberation mapping data of NGC 3227.

The main purpose of BELMAC is to model reverberation mapping data in order to infer or constrain the properties of the BLR, and hence the SMBH mass. To this end, we are working to integrate BELMAC into a parameter estimation procedure. To model a specific AGN, a user will need to provide the UV or optical continuum light curve (proxies for the ionizing continuum light curve), the observed velocity-resolved response of one or more BELs (i.e., a time sequence of spectra), estimates of the AGN's bolometric luminosity ($L_{\rm AGN}$) and the total ionizing photon luminosity ($Q_{\rm H}$), and a photoionization model grid computed with, ideally, the AGN's SED and an assumed set of chemical abundances. Given these inputs, BELMAC will produce a set of simulations sampling the parameter space, which the model optimization procedure will compare to the observed data to generate the posterior distributions for the free parameters (Section 2 and Figure 1) that control the BLR geometry, velocity field, gas cloud properties, and $M_\bullet$. Once this is implemented, BELMAC will be a valuable tool for BLR reverberation mapping modeling that will compliment existing modeling codes such as CARAMEL, MEMECHO, and BRAINS, while offering different capabilities.

5. Conclusion

We have presented a parameter exploration of velocity-resolved, reverberation response functions (numerical approximations of the transfer function) of the BLR using BELMAC. The main purpose of BELMAC is to serve as a versatile forward-modeling tool for analyzing BLR reverberation mapping data. BELMAC is designed for flexibility, allowing for various different combinations of geometry and dynamical models to be incorporated. Here, we focused on two distinct BLR models: a spherical shell with a radiation-pressure driven outflow, and a thin disk with Keplerian motion. In the models presented in this paper, the broad Hα line emission is calculated using an analytical prescription based on recombination theory. The main results of this paper are summarized below.

1. The τ–$v^{\parallel}$ relationship is linear for spherical radial outflows, and elliptical for rotating disks. This results in wedge-shaped and bell-shaped velocity-delay maps (2DRFs), respectively, as already described in earlier work (e.g., Pérez et al. 1992; Horne 1994; Pancoast et al. 2014).
2. For models with ICE and no matter-bounded clouds, the 1DRFs are flat-topped for spherical shell BLRs and double-peaked for disklike BLRs, for delays less than the light-crossing time of the inner cavity ($\tau \leqslant 1/Y_{\rm BLR}$). For $\tau > 1/Y_{\rm BLR}$, the 1DRFs for both shells and disks decay as τ increases, but the shape of the decay depends on the gas density profile and how the clouds are distributed. Whether for a sphere or a disk, the 1DRFs become more extended as s decreases and p increases ($\varepsilon_V(r)$ decreases more slowly with r). Additionally for the disk models, the time delay difference between the double peaks will reduce with decreasing inclination.
3. For models with ICE and no matter-bounded clouds, the time-averaged line profiles are flat-topped for spherical BLR models with radial outflows and double-peaked for rotating disk models. In spherical, radial outflow models, the response begins in the blue wing of the line profile, then propagates to the red wing. Therefore, the rms profiles tend to be skewed blueward, but the time-averaged line profiles are symmetric. In the rotating disk models, the response begins in the profile core, then propagates to the maximum velocity, $\pm v^{\parallel}_{\rm Kep}$, in the wings, and finally moves symmetrically back toward the core. The averaged line profiles have symmetrical double peaks, which have separations dependent on the disk's inclination. The rms profiles also have symmetrical double peaks; however, at large inclinations, the response amplitude at $v^{\parallel}_{\rm Kep} \approx 0$ km s^{-1} and $\tau \approx 0$ is strong enough that the rms spectra are triple-peaked.
4. We assume that recombination theory provides a reasonable estimation of the broad Hα response. Considering lines other than the hydrogen Balmer Series, the models with ICE can be considered to represent emission lines that are likely to be optically thin, such as CIV, and likewise, the ACE models represent lines, such as Lyα, that are likely to be optically thick.
5. Both matter-bounded clouds and ACE can affect the response quite dramatically because these effects suppress the response of the inner clouds, or the near-side clouds, respectively. Both effects cause the 1DRF to become more extended in time delay. The models with matter-bounded clouds respond as if the BLR has an effective inner radius that is greater than the true value of $R_{\rm in}$. In ACE models, the 1DRFs tend to peak at delays longer than $1/Y_{\rm BLR}$. In radial outflow models, ACE causes redward asymmetric line profiles. For rotating disks, the line and rms profiles decrease in amplitude by half, but ACE does not affect the shapes. However, matter-bounded clouds emit isotropically and therefore partly mitigate the profile asymmetry and decreased amplitude.
6. The luminosity-weighted radius is equivalent to the response-weighted delay when the BLR comprises entirely radiation-bounded, isotropically emitting clouds.

However, the RWD can significantly exceed the LWR when matter-bounded clouds are present or when clouds emit anisotropically. These effects in combination lead to overestimations of $R_{\rm BLR}$ by $\sim 10-100\%$, implying that measured cross-correlation lags may also overestimate $R_{\rm BLR}$ in such circumstances.

Acknowledgments

This paper is based upon work supported by the National Science Foundation under AARG/grant No. 2009508. This research has made use of NASA's Astrophysics Data System.

We thank the anonymous referee for providing constructive comments that have helped to improve the manuscript.

ORCID iDs

Sara A. Rosborough https://orcid.org/0000-0001-5055-507X
Andrew Robinson https://orcid.org/0000-0003-0672-2154
Triana Almeyda https://orcid.org/0000-0001-7259-7043

References

Alexander, D., & Hickox, R. 2012, NewAR, 56, 93
Almeyda, T., Robinson, A., Richmond, M., Vazquez, B., & Nikutta, R. 2017, ApJ, 843, 3
Almeyda, T., Robinson, A., Richmond, M., Nikutta, R., & McDonough, B. 2020, ApJ, 891, 26
Almeyda, T. R. 2017, PhD thesis, Rochester Institute of Technology
Amorim, A., Bauböck, M., Bentz, M. C., et al. 2021a, A&A, 654, A85
Amorim, A., Bauböck, M., Brandner, W., et al. 2020, A&A, 643, A154
Amorim, A., Bauböck, M., Brandner, W., et al. 2021b, A&A, 648, A117
Arav, N., Barlow, T. A., Laor, A., Sargent, W. L. W., & Blandford, R. D. 1998, MNRAS, 297, 990
Armijos-Abendaño, J., López, E., Llerena, M., & Logan, C. H. A. 2022, MNRAS, 514, 1535
Assef, R. J., Denney, K. D., Kochanek, C. S., et al. 2011, ApJ, 742, 93
Baskin, A., & Laor, A. 2018, MNRAS, 474, 1970
Baskin, A., Laor, A., & Stern, J. 2014, MNRAS, 438, 604
Batiste, M., Bentz, M. C., Raimundo, S. I., Vestergaard, M., & Onken, C. A. 2017, ApJL, 838, L10
Bentz, M. C., Denney, K. D., Grier, C. J., et al. 2013, ApJ, 767, 149
Bentz, M. C., & Katz, S. 2015, PASP, 127, 67
Bentz, M. C., Markham, M., Rosborough, S., et al. 2023, ApJ, 959, 25
Bentz, M. C., Walsh, J. L., Barth, A. J., et al. 2009, ApJ, 705, 199
Blandford, R. D., & McKee, C. F. 1982, ApJ, 255, 419
Davidson, K., & Netzer, H. 1979, RvMP, 51, 715
Di Matteo, T., Springel, V., & Hernquist, L. 2005, Natur, 433, 604
Dietrich, M., Wagner, S., Courvoisier, T. J., Bock, H., & North, P. 1999, A&A, 351, 31
Du, P., Hu, C., Lu, K.-X., et al. 2015, ApJ, 806, 22
Elitzur, M., Ho, L. C., & Trump, J. R. 2014, MNRAS, 438, 3340
Elvis, M. 2000, ApJ, 545, 63
Elvis, M. 2017, ApJ, 847, 56
Fabian, A. 2012, ARA&A, 50, 455
Fausnaugh, M. M., Grier, C. J., Bentz, M. C., et al. 2017, ApJ, 840, 97
Ferland, G. J., Chatzikos, M., Guzmán, F., et al. 2017, RMxAA, 53, 385
Goad, M. R., Korista, K. T., & Ruff, A. J. 2012, MNRAS, 426, 3086
Homayouni, Y., Trump, J. R., Grier, C. J., et al. 2020, ApJ, 901, 55
Hopkins, P. F., Hernquist, L., Cox, T. J., & Kereš, D. 2008, ApJS, 175, 356
Horne, K. 1994, in ASP Conf. Ser. 69, Proc. 10th RAL Workshop on Astronomy and Astrophysics, ed. P. M. Gondhalekar, K. Horne, & B. M. Peterson (San Francisco, CA: ASP), 23
Horne, K., Peterson, B., Collier, S., & Netzer, H. 2004, PASP, 116, 465
Jin, C., Ward, M., & Done, C. 2012, MNRAS, 425, 907
Koratkar, A. P., & Gaskell, C. M. 1991, ApJS, 75, 719
Kudoh, Y., Wada, K., Kawakatu, N., & Nomura, M. 2023, ApJ, 950, 72
Lawther, D., Goad, M. R., Korista, K. T., Ulrich, O., & Vestergaard, M. 2018, MNRAS, 481, 533
Li, Y.-R., Songsheng, Y.-Y., Qiu, J., et al. 2018, ApJ, 869, 137
Li, Y.-R., Wang, J.-M., Ho, L. C., Du, R., & Bai, J.-M. 2013, ApJ, 779, 110
Liu, X., Shen, Y., & Strauss, M. A. 2012, ApJ, 745, 94
Mangham, S. W., Knigge, C., Williams, P., et al. 2019, MNRAS, 488, 2780
Marconi, A., Axon, D., Maiolino, R., et al. 2008, ApJ, 678, 693
Marconi, A., Axon, D. J., Maiolino, R., et al. 2009, ApJL, 698, L103
Matthews, J. H., Knigge, C., Higginbottom, N., et al. 2020, MNRAS, 492, 5540
McConnell, N. J., & Ma, C.-P. 2013, ApJ, 764, 184
McLure, R. J., & Jarvis, M. J. 2002, MNRAS, 337, 109
Nenkova, M., Sirocky, M. M., Ivezić, Z., & Elitzur, M. 2008a, ApJ, 685, 147
Nenkova, M., Sirocky, M. M., Nikutta, R., Ivezić, Ž., & Elitzur, M. 2008b, ApJ, 685, 160
Netzer, H. 2008, NewAR, 52, 257
Netzer, H. 2020, MNRAS, 494, 1611
Netzer, H., & Marziani, P. 2010, ApJ, 724, 318
Osterbrock, D. E., & Mathews, W. G. 1986, ARA&A, 24, 171
Pancoast, A., Brewer, B. J., & Treu, T. 2011, ApJ, 730, 139
Pancoast, A., Brewer, B. J., & Treu, T. 2014, MNRAS, 445, 3055
Pérez, E., Robinson, A., & de La Fuente, L. 1992, MNRAS, 256, 103
Peterson, B. M., & Horne, K. 2004, AN, 325, 248
Proga, D., & Kallman, T. R. 2004, ApJ, 616, 688
Robinson, A. 1995, MNRAS, 272, 647
Robinson, A., & Perez, E. 1990, MNRAS, 244, 138
Shen, Y. 2013, BASI, 41, 61
Sturm, E., Dexter, J., Pfuhl, O., et al. 2018, Natur, 563, 657
Urry, C. M., & Padovani, P. 1995, PASP, 107, 803
Vestergaard, M., & Peterson, B. M. 2006, ApJ, 641, 689
Waters, T., Kashi, A., Proga, D., et al. 2016, ApJ, 827, 53
Welsh, W. F., & Horne, K. 1991, ApJ, 379, 586
Williams, P. R., & Treu, T. 2022, ApJ, 935, 128
Woo, J.-H., Yoon, Y., Park, S., Park, D., & Kim, S. C. 2015, ApJ, 801, 38
Yong, S. Y., Webster, R. L., King, A. L., et al. 2017, PASA, 34, e042